J. Fluid Mech. (2002), *vol.* 459, *pp.* 1–42. © 2002 Cambridge University Press
DOI: 10.1017/S0022112002007851 Printed in the United Kingdom

An investigation of stably stratified turbulent channel flow using large-eddy simulation

By VINCENZO ARMENIO[1] AND SUTANU SARKAR[2]

[1]Dipartimento di Ingegneria Civile, Università degli Studi di Trieste, Trieste, Italy

[2]Department of Mechanical and Aerospace Engineering University of California,
San Diego, CA 92093, USA

(Received 16 March 2001 and in revised form 19 October 2001)

Boundary-forced stratified turbulence is studied in the prototypical case of turbulent channel flow subject to stable stratification. The large-eddy simulation approach is used with a mixed subgrid model that involves a dynamic eddy viscosity component and a scale-similarity component. After an initial transient, the flow reaches a new balanced state corresponding to active wall-bounded turbulence with reduced vertical transport which, for the cases in our study with moderate-to-large levels of stratification, coexists with internal wave activity in the core of the channel. A systematic reduction of turbulence levels, density fluctuations and associated vertical transport with increasing stratification is observed. Countergradient buoyancy flux is observed in the outer region for sufficiently high stratification.

Mixing of the density field in stratified channel flow results from turbulent events generated near the boundaries that couple with the outer, more stable flow. The vertical density structure is thus of interest for analogous boundary-forced mixing situations in geophysical flows. It is found that, with increasing stratification, the mean density profile becomes sharper in the central region between the two turbulent layers at the upper and lower walls, similar to observations in field measurements as well as laboratory experiments with analogous density-mixing situations.

Channel flow is strongly inhomogeneous with alternative choices for the Richardson number. In spite of these complications, the gradient Richardson number, Ri_g, appears to be the important local determinant of buoyancy effects. All simulated cases show that correlation coefficients associated with vertical transport collapse from their nominal unstratified values over a narrow range, $0.15 < Ri_g < 0.25$. The vertical turbulent Froude number, Fr_w, has an $O(1)$ value across most of the channel. It is remarkable that stratified channel flow, with such a large variation of overall density difference (factor of 26) between cases, shows a relatively universal behaviour of correlation coefficients and vertical Froude number when plotted as a function of Ri_g. The visualizations show wavy motion in the core region where the gradient Richardson number, Ri_g, is large and low-speed streaks in the near-wall region, typical of unstratified channel flow, where Ri_g is small. It appears from the visualizations that, with increasing stratification, the region with wavy motion progressively encroaches into the zone with active turbulence; the location of $Ri_g \simeq 0.2$ roughly corresponds to the boundary between the two zones.

---

1. Introduction

The study of stratified turbulent shear flows is relevant to many applications in environmental and geophysical flows. Stratification leads to qualitative and quantitative changes in the small-scale mixing of momentum, salinity, pollutant and nutrients which must be understood and, furthermore, parameterized in large-scale circulation models. Turbulence in geophysical flows has a wide variety of sources, for example, see Caldwell (1987) and Caldwell & Moum (1995) for a discussion in the context of ocean microstructure. Often, the forcing involves boundaries: the wind-driven upper mixed layer; the bottom boundary layer, especially in shallow coastal waters; side boundaries in estuaries, tidal channels and bays; as well as separated flows over sills, seamounts and at the coastline. Of the many past experimental and numerical investigations of turbulent transport and mixing in a stably stratified medium, the predominant majority has dealt with flows away from boundaries. However, as discussed above, there are situations where boundaries are important determinants of mixing.

Perhaps the question of the most global importance in stratified shear flows is how does the turbulence level and associated mixing in shear flows change when the stratification, measured by an appropriate parameter, increases. This information is not only key to our knowledge of stratified flow physics but also critical to predictive models of ocean/atmospheric mesoscales where stratification effects on the microstructure must necessarily be parameterized. The primary external parameter associated with stratification in shear flows is the gradient Richardson number, $Ri_g = N^2/S^2$, where N is the Brunt–Väisälä frequency and S is the mean shear rate. The following brief literature survey indicates that, while our understanding of the Richardson number dependence is fair in free shear flows, it is poor in the case of wall-bounded flows.

Linear inviscid stability analysis by Miles (1961) gives $Ri_g \geqslant 0.25$ as a sufficient condition for stability of a sheared stratified flow. The analogous criterion for the fate of large-amplitude nonlinearly evolving disturbances is of great interest and has been studied in various configurations as discussed below.

Uniformly sheared flow in a fluid with linear stratification has been extensively studied because the spatially constant value of Ri_g in such a flow leads to considerable simplification. Rohr *et al.* (1998) performed laboratory experiments using a salt-stratified water channel. The critical value, $Ri_{g,cr}$, is defined to be the value of gradient Richardson number where a constant level of velocity fluctuations is obtained; these fluctuations decay for $Ri_g > Ri_{g,cr}$ whereas turbulence grows for $Ri_g < Ri_{g,cr}$. The results of Rohr *et al.* (1988) show that $Ri_{g,cr} = 0.25 \pm 0.05$. Further experimental studies were performed using a thermally stratified facility by Piccirillo & Van Atta (1995), DNS was performed by Gerz, Schumann & Elghobashi (1989), Holt, Koseff & Ferziger (1992), Jacobitz, Sarkar & Van Atta (1997), Jacobitz & Sarkar (1999) and Diamessis & Nomura (2000), and LES by Kaltenbach, Gerz & Schumann (1994). One conclusion of these studies is that the value of $Ri_{g,cr}$ depends on other parameters. It increases with Reynolds number, asymptoting to a constant value. The value of $Ri_{g,cr}$ is also a function of shear number, Sk/ϵ (with k the turbulent kinetic energy and ϵ the dissipation rate), as shown in a systematic study by Jacobitz *et al.* (1997) using DNS. At sufficiently large values of Sk/ϵ, linear effects persist leading to anomalously low turbulence growth rates. The shear number effect over a range of initial Reynolds numbers, $Re_\lambda = 22$, 44 and 88 was studied by Jacobitz & Sarkar (1999) who found that the value of SK/ϵ required for the persistence of linear effects increases with Reynolds number. Shih *et al.* (2000) also found a shear number effect at moderate values of Re_λ; however, their series at $Re_\lambda = 88$ did not extend to a sufficiently large value of SK/ϵ for the shear number effect to be important. To summarize, for moderate values of the shear number and sufficiently large Reynolds number, the observed values of $Ri_{g,cr}$ in the range $0.18 < Ri_{g,cr} < 0.25$ are consistent with the linear analysis result that $Ri_g > 0.25$ is a sufficient condition for stability.

The shear layer developing between two streams of different velocity and different densities is a model problem of great interest because the Kelvin–Helmholtz billows and subsequent secondary instabilities are found to correlate with ocean microstructure in field data. Laboratory experiments by Thorpe (1973), Koop & Browand (1979) and, more recently, numerical simulations by Caulfield & Peltier (2000), Smyth & Moum (2000) and Staquet (1995) have investigated the evolution of the stratified shear layer. During the evolution of the shear layer, the Richardson number increases and, eventually, further thickness growth by turbulent entrainment is suppressed; the centreline value of Ri_g associated with such suppression has values similar to that of $Ri_{g,cr}$ in uniformly sheared flow.

Relative to free shear flows, few investigations of stratified wall-bounded flows have been performed. The qualitative difference between the inner and outer layers of turbulent wall-bounded flows along with the spatial inhomogeneity of the flow introduces different Richardson numbers (see §§ 3.1 and 3.2 for pertinent definitions) as relevant parameters. The buoyancy flux in stratified boundary layers is boundary-driven with the turbulence originating near the wall where the gradient Richardson number, Ri_g, is small, and then passing to the outer, less-active region where the local values of Ri_g are large.

Oceanic measurements of turbulence quantities in stratified wall-bounded situations are relatively scarce because of difficulties in performing such measurements. Recently, Lu, Lueck & Huang (2000) have reported turbulence measurements in the Cordova Channel, a tidal channel of 30 m depth. Stratification levels as measured by Ri_g were found to be significant and to cause lower mixing lengths and transport coefficients relative to values expected for unstratified flow. Mean velocity profiles were found to be fitted by a log-law. Stacey, Monismith & Burau (1999) have measured profiles of Reynolds stress in the northern San Francisco Bay. The effect of stable stratification was found to be strong during weak ebb/flood tides and to confine active turbulence to a region near the bottom boundary away from the upper, largely inactive zone.

The atmospheric boundary layer under both convective and stable conditions has been previously investigated. Field observations of the vertical variation of vertical fluxes, mean velocity and mean temperature indicate that the upper portion that caps the stable boundary layer has significant wave activity and intermittency. Large-eddy simulation (LES) of the stable atmospheric boundary has been performed by Mason & Derbyshire (1990) and Saiki, Moeng & Sullivan (2000) with eddy-diffusivity type models. Mason & Derbyshire (1990) used the Smagorinsky model with a modification dependent on the subgrid value of the flux Richardson number, Ri_f, while Saiki *et al.* (2000) use an additional transport equation for the subgrid kinetic energy. Kosovic & Curry (2000) use a nonlinear (quadratic in strain rate) eddy diffusivity model, a transport equation for the subgrid kinetic energy, and assign a fixed fraction of the net energy transfer to backscatter. A bottom boundary layer capped by an upper region with internal wave activity is observed by Kosovic & Curry (2000) and Saiki *et al.* (2000) in their simulations.

Experimental investigations of stratified wall-bounded turbulence were performed by Arya (1975), Piat & Hopfinger (1981), Britter (1974), Komori (1980) and Komori *et al.* (1983) (hereafter the last two works are referred to as KUOM). Arya considered a stratified boundary layer of air developing over a cooled/heated wall and, in the stably stratified regime, increased the overall Richardson number, $Ri_\delta = (g\delta\Delta\rho)/(\rho_0 u_\infty^2)$, with δ the boundary layer thickness and U_∞ the free-stream velocity, up to $Ri_\delta = 0.098$. It was found that stable stratification reduces both the skin friction coefficient and the Nusselt number as well as suppresses turbulence intensities. No relaminarization of the flow was observed in the range of Richardson numbers investigated by Arya (1975). Britter (1974) studied a channel flow with heated top wall and adiabatic bottom wall. A large reduction in the Nusselt number was observed at high levels of overall stratification. The experiments of KUOM were performed by condensing steam over the upper surface in an open-channel flow. The bulk Richardson number, $Ri_b = (gR\Delta\rho)/2\rho_0 u_b^2$ with R the hydraulic radius and u_b the bulk (average over the cross-section) velocity, was varied up to $Ri_b = 0.135$. Turbulence levels and the buoyancy flux were found to exhibit a general reduction with increasing stratification. Again, no relaminarization was observed. KUOM found that, under strong stratification, a wave-like motion occurs in the core of the channel together with countergradient momentum and heat fluxes. When the outer-layer quantities are plotted as a function of the *local* gradient Richardson number, it was found that the correlation coefficients associated with the Reynolds shear stress decreased sharply at $Ri_g \simeq 0.1$ and approached zero at values of approximately $Ri_g \simeq 0.2 - 0.3$.

Recently Garg (1996) and Garg *et al.* (2000) (henceforth both referred to as GFMK) performed LES and DNS of a stratified, incompressible turbulent channel flow. The Boussinesq form of the governing equations was used and a dynamic eddy-viscosity model was employed for the parameterization of the subgrid-scale stresses and density fluxes. The equations were solved with a hybrid spectral finite-difference discretization and a fractional-step algorithm. The mean pressure gradient that drives the flow was kept constant. In addition to closed-channel flow, open channel flow was also simulated by the authors. In the case of closed channel flow, the authors investigated the range of Richardson numbers, $0 \leqslant Ri_\tau \leqslant 60$, in a flow with $Re_\tau = 180$ and obtained interesting results. Three regimes depending on the friction Richardson number $Ri_\tau = \Delta\rho g h/\rho_0 u_\tau^2$ (with u_τ denoting the friction velocity) were identified: for $Ri_\tau < 30$, there is a *buoyancy-affected* regime (BA) in which turbulence is suppressed but still active; for $30 < Ri_\tau < 45$, there is a *buoyancy-controlled* regime with relaminarization of one half of the channel during the early stage of the simulation followed by sharp transition that restores a symmetric turbulent flow; for $Ri_\tau > 45$, there is a *buoyancy-dominated* regime (BD) characterized by rapid relaminarization of the whole flow. Unlike previous investigations, it was concluded that the friction Richardson number is better suited for the characterization of the flow regimes than the gradient Richardson number.

Criteria for the stability of stratified wall-bounded flows to linearly evolving disturbances were obtained by Gage & Reid (1968) and Gage (1971). The analysis of Gage & Reid (1968) for plane Poiseuille flow with a linear density profile (Prandtl number of unity) showed that the critical Richardson number increases with increasing Reynolds number. For infinite Reynolds number, it was found that channel flow is linearly stable for $Ri_c > 0.0554$. In that study, the Richardson number is defined as $Ri_c = gh\Delta\rho/8\rho_0 u_c^2$ where g is the gravitational acceleration, h is the channel half-height, $\Delta\rho$ is the difference between density values at the walls, ρ_0 is a reference density and u_c is the centreline velocity. Note that Ri_c is equal to the minimum value of the usual gradient Richardson number, $Ri_g = N^2/S^2$, associated with the base flow.

The literature survey, summarized above, reveals the following open issues regarding channel flow subjected to stable stratification.

(*a*) The numerical results of GFMK regarding the state of fluctuating motion at strong stable stratification are not consistent with the results of linear theory, laboratory experiments, and field observations. The linear analysis of Gage & Reid (1968) gives the value of the critical Richardson number required for a stratified channel flow to remain laminar as a function of Reynolds number. It is shown in § 3.4 that, for the case with $Re_\tau = 180$ considered by GFMK, the corresponding laminar flow would be linearly unstable for $Ri_\tau < 881$. On the other hand, the value of $Ri_\tau \simeq 45$ is quoted by GFMK as the value at which the flow relaminarizes. Laboratory experiments, as discussed more fully in § 3.3 that summarizes the results of KUOM, do not show complete relaminarization in wall-bounded turbulence, for stratification levels equivalent to that in GFMK. For example, turbulence in the inner layer along with a wave-like motion in the outer layer is observed for very strong stratification by KUOM. Field observations such as those of Stacey *et al.* (1999) also show active turbulence in a bottom boundary layer coexisting with an upper zone consisting of suppressed, inactive fluctuating motion.

(*b*) The experimental investigations of wall-bounded flows (for example see Arya 1975; Komori *et al.* 1983), studies of stratified shear flows in general, and parameterizations of environmental and geophysical flows emphasize the gradient Richardson number or the Monin–Obukhov length. However, other parameters such as the friction Richardson number have also been used.

In the light of the above issues, we revisit the problem of stably stratified channel flow by performing a LES study. The major questions motivating our study are: (*a*) What is the state of fluctuating motion as a function of overall stable density difference, and (*b*) is the local gradient Richardson number a good local determinant of the state of the flow and associated turbulent transport? These questions are of course generic to a broad class of wall-bounded stably stratified flows. The simulated cases in our LES study span a wide range of stratifications, $0 < Ri_b < 0.593$. The centreline Reynolds number varies in the range $3240 < Re_c < 7149$ while the nominal friction Reynolds number is $Re_\tau = 180$.

The present study focuses on the response of initially turbulent flow subjected to stable stratification. The development of an initially laminar flow with corresponding parabolic velocity profile and a linear density profile is also important, but is a distinct problem involving laminar-to-turbulent transition that deserves a separate investigation. Uniform shear flow with isotropic turbulence as initial conditions has been shown by Rohr *et al.* (1988) to exhibit three asymptotic states of fluctuating motion, i.e. growth, constant value, or decay depending on whether the value of Ri_g is less than, equal to, or greater than the critical value, $Ri_{g,cr}$. The DNS of the initially laminar shear layer by Smyth & Moum (2000) shows that the same three regimes are visited in sequence when the shear layer thickness and the value of Ri_g increase in time. Both uniform shear flow and the shear layer, also exhibit similar values of the gradient Richardson number, $Ri_{g,cr} \simeq 0.25$. Based on the free shear flow cases, perhaps in the case of wall-bounded flows there is a similar correspondence between the problem with laminar initial conditions and that with turbulent initial conditions.

The paper is organized as follows. The next section contains the mathematical model together with a brief description of the SGS models and the algorithm used for the integration of the filtered equations. Section 3 gives theoretical background necessary to interpret the results. Sections 4 and 5 describe the results of our simulation. A discussion of these results is finally reported in § 6.

2. Mathematical model

2.1. *Governing equations*

In the present paper we consider a turbulent plane channel flow. In order to conform with the numerical study of GFMK as well as the experimental investigation of KUOM, a relatively low Reynolds number flow is simulated, $Re_\tau = u_\tau h/\nu = 180$, based on the channel half-height h and the friction velocity $u_\tau = \sqrt{\tau_w/\rho_0}$ with τ_w the wall stress and ρ_0 a reference density. Following the recent DNS study of Moser, Kim & Mansour (1999), the computational domain is $L_x = 4\pi h$ long in the streamwise (x) direction, $L_y = (4/3)\pi h$ wide in the transverse (y) direction, and $2h$ high in the vertical (z), wall-normal direction. A constant pressure gradient drives the flow and a stable stratification is maintained by imposing a constant upper-wall density which is smaller than the constant bottom-wall density. The total density field is

$$\rho^*(x,y,z,t) = \rho_0 + \rho(x,y,z,t)$$

with

$$\rho(x,y,z,t) = \rho_b(z,t) + \rho'(x,y,z,t).$$

Here $\rho_b(z,t)$ is the mean, bulk density profile that is a function of the vertical space coordinate and is obtained by plane-averaging over the (x,y)-planes of homogeneity, while $\rho'(x,y,z,t)$ is the fluctuating three-dimensional field.

Under the assumption that the density variation is small with respect to the reference density ρ_0, the Boussinesq approximation holds and the density in the inertial term is taken to be constant, $\rho^* = \rho_0$. The filtered governing equations can be written as follows:

$$\frac{\partial \overline{u_i}}{\partial x_i} = 0, \tag{2.1}$$

$$\frac{\partial \overline{u_i}}{\partial t} + \frac{\partial \overline{u_j}\,\overline{u_i}}{\partial x_j} = -\frac{\partial \bar{p}}{\partial x_i} + \frac{1}{Re}\frac{\partial}{\partial x_j}\frac{\partial \overline{u_i}}{\partial x_j} + F\delta_{i1} - Ri(\bar{\rho} - \bar{\rho}_b)\delta_{i3} - \frac{\partial \tau_{ij}}{\partial x_j}, \tag{2.2}$$

$$\frac{\partial \bar{\rho}}{\partial t} + \frac{\partial \overline{u_j}\bar{\rho}}{\partial x_j} = k\frac{\partial}{\partial x_j}\frac{\partial \bar{\rho}}{\partial x_j} - \frac{\partial \lambda_j}{\partial x_j}. \tag{2.3}$$

In (2.1)–(2.3), $\overline{u_i}$ is the i-component of the filtered velocity field made dimensionless with a reference velocity u_r, $\bar{p}$ denotes the filtered pressure field (non-dimensionalized by $\rho_0 u_r^2$) that remains after removing the component that is in hydrostatic balance with the bulk density field, the density difference appearing in the buoyancy term is normalized by an appropriate scale $\Delta\rho$, F is the constant driving force, i.e. the imposed non-dimensional mean pressure gradient, τ_{ij} and λ_j are the subgrid-scale (SGS) stress and density flux, respectively, which need to be modelled, and $k = \nu/Pr$ is the molecular diffusivity of the density field. The non-dimensional parameters are as follows: $Re = u_r h/\nu$ is the reference Reynolds number, Pr is the reference Prandtl number and $Ri = \Delta\rho g h/\rho_0 u_r^2$ is the reference Richardson number. In the present simulations, we use $Pr = 0.71$ corresponding to thermally stratified air. Simulations at higher Prandtl number are desirable in the future since, in oceanic flows, $Pr = 5$ and 700 for heat and salt, respectively.

We use a dynamic mixed model for the momentum equation that recently has been shown to be very effective in equilibrium as well as non-equilibrium wall-bounded flows by Armenio & Piomelli (2000), whereas a dynamic eddy-viscosity model, previously used with success by Le Reibault, Sarkar & Stanley (2001) is used for the density equation. In particular, the SGS stresses are modelled using a mixed model composed of a scale-similar part (Bardina, Ferziger & Reynolds 1980) and an eddy viscosity part introduced by Smagorinsky (1963):

$$\tau_{ij} = (\overline{\bar{u}_i\bar{u}_j} - \bar{\bar{u}}_i\bar{\bar{u}}_j) - 2C\bar{\Delta}^2|\bar{S}|\bar{S}_{ij}, \tag{2.4}$$

where $\overline{S}_{ij}$ is the resolved strain rate tensor and $S = \sqrt{2S_{ij}S_{ij}}$. The coefficient C in (2.4) is evaluated dynamically following Germano *et al.* (1991) using the Germano identity $L_{ij} = \Sigma_{ij} - \widehat{\tau}_{ij}$, where $L_{ij} = \widehat{\bar{u}_i\bar{u}_j} - \hat{\bar{u}}_i\hat{\bar{u}}_j$ denotes the resolved turbulent stress tensor and Σ_{ij} the subtest-scale stresses. When using the least-squares procedure for the mixed model, (2.4), the coefficient C is given by

$$C = -\frac{1}{2}\frac{\langle L_{ij}M_{ij}\rangle - \langle N_{ij}M_{ij}\rangle}{\langle M_{mn}M_{mn}\rangle}. \tag{2.5}$$

In (2.5) we have

$$M_{ij} = \hat{\bar{\Delta}}^2|\hat{\bar{S}}|\hat{\bar{S}}_{ij} - \widehat{\bar{\Delta}^2|\bar{S}|\bar{S}_{ij}}, \tag{2.6}$$

$$N_{ij} = \left(\widehat{\overline{\hat{\bar{u}}_i\hat{\bar{u}}_j}} - \hat{\bar{\hat{\bar{u}}}}_i\hat{\bar{\hat{\bar{u}}}}_j\right) - \left(\widehat{\overline{\bar{u}_i\bar{u}_j}} - \hat{\bar{\bar{u}}}_i\hat{\bar{\bar{u}}}_j\right). \tag{2.7}$$

A dynamic eddy diffusivity model for scalar transport has been used with success previously, for example in a jet by Le Reibault *et al.* (2001). Such a model for the subgrid density flux reads

$$\lambda_j = -C_\rho\bar{\Delta}^2|\bar{S}|\frac{\partial\bar{\rho}}{\partial x_j}. \tag{2.8}$$

Similar to the momentum equation, the constant C_ρ is evaluated dynamically using a test filter and a grid filter:

$$C_\rho = -\frac{1}{2}\frac{\langle \mathscr{L}_i\mathscr{M}_i\rangle}{\langle \mathscr{M}_k\mathscr{M}_k\rangle}, \tag{2.9}$$

with $\mathscr{M}_i = \hat{\bar{\Delta}}^2|\hat{\bar{S}}|\widehat{\partial\bar{\rho}/\partial x_i} - \widehat{\bar{\Delta}^2|\bar{S}|\partial\bar{\rho}/\partial x_i}$ and $\mathscr{L}_i = \widehat{\bar{\rho}\,\bar{u}_i} - \hat{\bar{\rho}}\,\hat{\bar{u}}_i$.

Filtering is performed in all three directions which, according to Armenio & Piomelli (2000), gives good results in neutral channel flow. In the above equations $\langle\cdot\rangle$ denotes an appropriate ensemble required to avoid the mathematical inconsistency that one encounters when C or C_ρ are removed outside the filtering operation during the dynamic procedure. Since the flow is homogeneous in the (x, y)-planes, plane-averaging of the dynamic coefficients, C and C_ρ, is applicable and used. In order to avoid unphysically large back-scattering, the dynamic coefficients are set to zero during the rare occasions when they reach negative values. However, physical backscatter is allowed by the scale-similar part of the SGS model.

2.2. *Numerical method*

The Navier–Stokes equations together with the density equation are solved using the semi-implicit, fractional-step algorithm recently developed by Zang, Street & Koseff (1994). The Adams–Bashforth technique is used for the time advancement of the convective terms, whereas the diffusive terms are treated implicitly with the Crank–Nicolson scheme. The space derivatives are discretized with the second-order centred scheme, thus the algorithm is overall second-order accurate both in time and in space. A multigrid technique is used for the solution of the pressure equation. The algorithm has been demonstrated to be second-order accurate for mass, momentum and energy conservation by Armenio & Piomelli (2000). Since the turbulent field is homogeneous in the streamwise as well as in the transversal direction, periodic boundary conditions are used in the (x, y)-coordinates for the velocity field, the pressure and the density. At the rigid walls, the no-slip condition is used for the velocity field. The density is kept constant at the walls, with ρ_{bot} and ρ_{top} denoting the values at the bottom and top walls, respectively.

The algorithm has been extensively validated against DNS data and LES data of other authors. Details are reported in Appendix A. Furthermore, the performance of the SGS models is discussed in Appendix B. The 'fine' grid of table 2, Appendix A, is used for the results shown here.

3. Theoretical background

3.1. *Inner and outer scales*

It is well known that wall-bounded turbulent flows have two distinct regions: an inner near-wall layer and an outer layer. In presenting results, outer-scale quantities or inner-scale quantities will be used as appropriate for normalization. Outer-scale quantities are centreline mean velocity, u_c, bulk velocity, u_b, or the imposed density difference, $\Delta\rho$. The bulk velocity, $u_b = (1/A)\int u \, \mathrm{d}A$, is an area-averaged measure of the channel velocity. The inner-scale velocity is the friction velocity,

$$u_\tau = \sqrt{\tau_w/\rho},$$

whereas the corresponding scale for the density is the friction density,

$$\rho_\tau = \frac{Q_w}{u_\tau} = \frac{-k(\partial\langle\rho\rangle/\partial z)_w}{u_\tau}, \tag{3.1}$$

where Q_w is the density flux at the wall and $k = \nu/Pr$ is the molecular diffusivity of density. The friction density is a normalized wall density flux just as the friction velocity is a normalized wall stress. An important non-dimensional number which will be referred to throughout the paper is the Nusselt number:

$$Nu = \frac{2hQ_w^{av}}{k\Delta\rho}, \tag{3.2}$$

with $Q_w^{av} = (1/2)(Q_{top} + Q_{bot})$. In the case of purely diffusive mass transport through a stationary fluid, $Nu = 1$; thus the value of Nu quantifies the increase of wall mass transport due to turbulence with respect to its laminar value.

3.2. *Richardson numbers in channel flow*

It is tempting to parameterize the flow using a single, overall Richardson number. One possibility is to use the outer velocity scale, for example the bulk Richardson number (KUOM),

$$Ri_b = \frac{\Delta\rho g h}{2\rho_0 u_b^2}, \tag{3.3}$$

where u_b is the bulk (average) velocity based on flow rate and cross-sectional area. The choice of u_b could be replaced by the free-stream velocity, u_∞, in a developing boundary layer, for example by Arya (1975) or by the centreline velocity, u_c, in channel flow as done by Gage & Reid (1968). Another possibility is to use an inner velocity scale and define a friction Richardson number (GFMK),

$$Ri_\tau = \frac{\Delta\rho g h}{\rho_0 u_\tau^2}. \tag{3.4}$$

The definition of Ri_τ involves an outer-scale quantity for the density variation but an inner-scale quantity for the velocity variation. The relationship between the friction and bulk Richardson numbers is

$$Ri_\tau = 2Ri_b \frac{u_b^2}{u_\tau^2}. \tag{3.5}$$

The friction Richardson number is much larger in magnitude than the bulk Richardson number and explicitly involves viscosity.

In unbounded shear flows, the gradient Richardson number, $Ri_g = N^2/S^2$, has been established as the key parameter, based on mean quantities, that determines the influence of stratification. We now estimate values of Ri_g at key locations. The shear at the wall is u_τ^2/ν while, from (3.2), the mean density gradient at the wall is $(Nu\Delta\rho)/(2h)$ giving the wall value of the gradient Richardson number as

$$Ri_g(z=0) = Ri_\tau \frac{Nu}{2Re_\tau^2}, \tag{3.6}$$

which is a small quantity at high Reynolds number because of the inverse-square dependence on Re_τ. The variation of Ri_g across the channel can be estimated after approximating the mean velocity and mean density profiles by classical log-layer scaling; the shear is $u_\tau/\kappa z$ and the mean density gradient is $\rho_\tau/\kappa_\rho z$ with κ the von Kármán constant and κ_ρ the equivalent constant for the mean density profile. After using (3.1)–(3.2), and some algebraic manipulation the following result is obtained:

$$Ri_g(z) = Ri_\tau \frac{Nu\kappa^2}{2PrRe_\tau\kappa_\rho}\frac{z}{h}. \tag{3.7}$$

Thus log-layer scaling implies that $Ri_g(z)$ increases linearly in the vertical direction and that, in the core of the channel where $z = O(h)$, the value of the gradient Richardson number exceeds the wall value, $Ri_g(0)$ given by (3.6), by a large multiple, $O(Re_\tau)$. The gradient Richardson number becomes singular at the centre of the channel or at the edge of the boundary layer where the mean shear vanishes.

3.3. *Implications of the experiments of KUOM*

KUOM have performed experiments using an open water-channel flow ($Pr \sim 5$) for both stable and unstable stratification. In their investigation, the free-surface Froude number was very small, and consequently the effect of surface waves was negligible. In the case of stable stratification, they considered relatively small-Reynolds-number flows and a wide range of bulk Richardson numbers ranging between neutral flow ($Ri_b = 0$) and a strongly stratified case ($Ri_b = 0.135$). The above numbers are quoted by the authors using the hydraulic radius of the section which, in the limiting case of infinite span, collapses to the height of the open channel. The Reynolds number in the experiments of KUOM spans the range $140 < Re_\tau < 226$.

Since an open channel flow is similar to half of a closed channel flow, an analogy can be drawn between the two flows. An open channel with height h and zero stress at the free surface experiences the same friction velocity, u_τ, as a closed channel flow with height $2h$, and the two flows are equivalent in terms of viscous wall stress.

Using the data tabulated by KUOM, values of the friction Richardson number can be obtained from

$$Ri_{\tau,KUOM} = \frac{(\rho_{bot} - \rho_{fs})gh}{\rho_0 u_\tau^2},$$

with ρ_{fs} and ρ_{bot} denoting the density at the free surface and bottom wall, respectively. In the equivalent closed channel, the centreline value of mean density must be the same as ρ_{fs}, so that the imposed density difference, $\rho_{bot} - \rho_{top}$, in the equivalent closed channel is equal to $2(\rho_{bot} - \rho_{fs})$. Therefore the Richardson number of the equivalent closed channel is

$$Ri_{\tau,cc} = \frac{(\rho_{bot} - \rho_{top})gh}{\rho_0 u_\tau^2} = \frac{2(\rho_{bot} - \rho_{fs})gh}{\rho_0 u_\tau^2} = 2Ri_{\tau,KUOM}. \tag{3.8}$$

KUOM show that at $Ri_b = 0.135$, equivalent to $Ri_{\tau,KUOM} = 73$, and Reynolds number, $Re_\tau = 226$, two distinct zones are detected: the inner layer in which turbulence is reduced but still active, and the outer layer where large internal waves occur that periodically break and generate strong intermittency. Referring to (3.8), it appears that an equivalent closed channel flow would experience a qualitatively similar behaviour for $Ri_\tau = 146$.

3.4. *Implications of linear theory*

As stated in the introduction, a linear theory has been developed by Gage & Reid (1968) who find an explicit relation between the critical Richardson number for stability and the Reynolds number of the flow. In their analysis, the authors considered a stably stratified channel flow with imposed temperatures at the walls, equivalent to the problem under investigation in the present paper. They use the centreline Richardson number defined by

$$Ri_c = \frac{g2h\Delta\rho}{\rho_0 16 u_c^2}, \tag{3.9}$$

which can be related to the friction Richardson number to give

$$Ri_\tau = 8Ri_c \frac{u_c^2}{u_\tau^2} = 8Ri_c \frac{Re_c^2}{Re_\tau^2}. \tag{3.10}$$

In a laminar plane Poiseuille flow, the velocity is parabolic giving that

$$\left.\frac{\mathrm{d}u}{\mathrm{d}z}\right|_{wall} = \frac{2u_c}{h}$$

$$\Rightarrow \frac{u_\tau^2}{\nu} = \frac{2u_c}{h}$$

$$\Rightarrow \frac{Re_\tau^2}{2} = Re_c.$$

Therefore, (3.10) becomes

$$Ri_\tau = 2Ri_c Re_\tau^2. \tag{3.11}$$

Table 1 of Gage & Reid (1968) with $Re_c = 16\,200$ (corresponding to the value $Re_\tau = 180$ in the LES) gives the critical value of the Richardson number beyond which the flow is laminar to be $Ri_c = 0.0136$. With these values, (3.11) implies that laminar plane Poiseuille flow corresponding to $Re_\tau = 180$ is linearly stable if

$$Ri_\tau > 881. \tag{3.12}$$

Case	Ri_τ	Ri_b	Re_τ	Re_b	Re_c	$c_f \times 10^3$	*Nu*
C0	0	0.0	180	2800	3240	8.18	5.95
C1	18	0.032	180	3102	3764	6.73	3.71
C2	60	0.0685	183	3666	4743	4.99	2.79
C3	120	0.112	180	4154	5623	3.71	2.27
C4	240	0.188	181	4567	6224	3.14	1.70
C5	480	0.297	178	5120	7149	2.40	1.28

TABLE 1. Important quantities that characterize the state of stratified channel flow. Ri_τ is the friction Richardson number imposed on the flow at $t = 0$ which is also the expected theoretical value at the final steady state. Subsequent columns correspond to the final steady state.

GFMK find that the $Re_\tau = 180$ case laminarizes at $Ri_\tau \simeq 45$. However, the corresponding laminar profile would be unstable to small disturbances at this Richardson number, in view of (3.12). Moreover, it should be remarked that if finite-amplitude disturbances induce subcritical transition Kleiser & Zang (1991), the value of Ri_τ required to relaminarize the flow may be even larger than 881. The GFMK result of a laminar steady state at $Ri_\tau \simeq 45$ appears to be inconsistent with linear theory.

According to Gage & Reid (1968), the critical value of the centreline Richardson number defined by (3.9) is found to increase as a function of Reynolds number and finally asymptotes to the value

$$Ri_c = 0.0554 \tag{3.13}$$

at infinite Reynolds number. Assuming a parabolic velocity profile so that the bulk velocity is $u_b = 2u_c/3$, where u_c is the centreline velocity, it follows that channel flow is linearly stable if

$$Ri_b > 0.5,$$

where the bulk Richardson number is defined by (3.3).

4. Transient development of the flow in the presence of stable stratification

The most convenient method of investigating stratified channel flow driven by a constant mean pressure gradient is to vary the reference Richardson number in the governing equations so as to impose target values of the friction Richardson number, Ri_τ, at $tu_\tau/h = 0$. The second column in table 1 lists these values of Ri_τ while subsequent columns in the table refer to the final values of quantities important to characterize the overall state of the flow. We defer the discussion of these final values to § 5 and, instead, summarize the transient evolution of the flow.

As outlined previously, GFMK have shown the existence of different turbulent regimes based on the magnitude of the friction Richardson number; our choices of Ri_τ overlap with the values chosen by GFMK. They started the simulations from a realization of equilibrium channel flow with a passive scalar, which motivated our choice of passive-scalar initial conditions for cases C1 and C2. Case C1 has the low value of $Ri_\tau = 18$ corresponding to the buoyancy-affected regime of GFMK. Case C2 corresponds to a case investigated by GFMK and identified as buoyancy-dominated. Cases C3–C5 have higher stratification than covered by GFMK, with C3 having a value of bulk Richardson number, $Ri_b = 0.112$, near the high end of the cases studied in KUOM. The initial condition for case C3 is chosen to be a realization from the

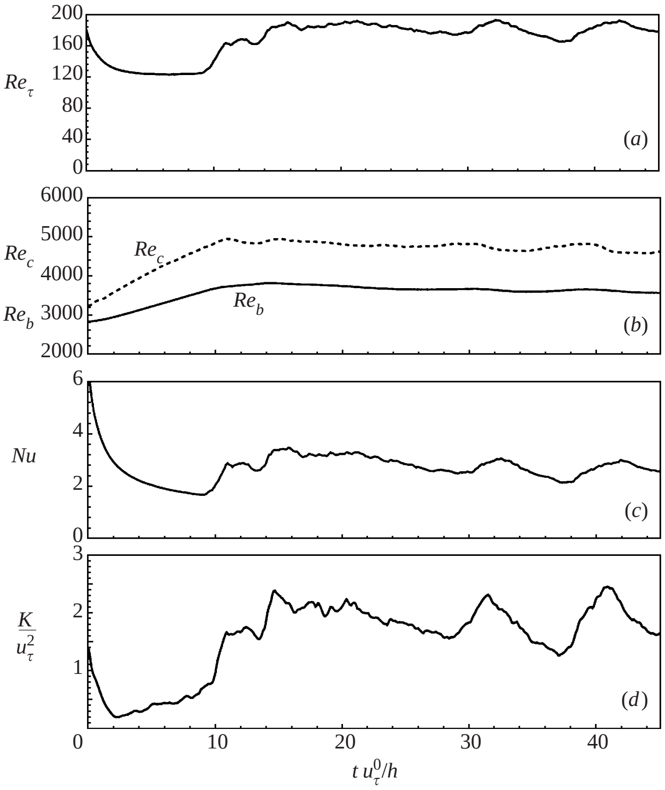

FIGURE 1. Time evolution of bulk quantities for $Ri_\tau = 60$, starting from the passive scalar case: (*a*) friction Reynolds number; (*b*) bulk and centreline Reynolds numbers; (*c*) Nusselt number; (*d*) turbulent kinetic energy averaged over the whole channel.

final steady state of case C2. Similarly, the initial condition for case C4 is chosen from the final steady state of case C3 and that of case C5 chosen from final state of case C4. Such a choice of initial conditions is motivated by a desire to keep the transient short as discussed in Appendix C.

The pressure gradient, F, that drives the flow is kept constant and due to the integral balance between the pressure gradient and the viscous wall friction at steady state

$$2hF = (\tau_{top} + \tau_{bot}), \tag{4.1}$$

the steady-state value of the friction Reynolds number, $Re_\tau = u_\tau h/\nu$, must approach its initial value after an initial transient. The simulations are run for the time, which is relatively long in wall units, necessary to achieve convergence to the theoretically expected steady-state value of $Re_\tau \simeq 180$, and then statistics are obtained by time-averaging over a sufficiently long interval.

4.1. *Moderate-Richardson-number cases*

The transient development in case C2 which is representative of all the simulations with $Ri_\tau \geqslant 60$ is discussed here. The flow develops from an initial state of fully developed channel flow with density fluctuations corresponding to a passive scalar field. Figure 1 shows the time-evolution of the main bulk quantities for case C2. In agreement with GFMK, it appears that when stable stratification is imposed a transient, characterized by a dramatic decrease of the wall stress, occurs as shown in figure 1(*a*). Corresponding to the reduction of wall friction, the flow accelerates since the driving pressure gradient is held constant, and consequently, the bulk Reynolds number increases in figure 1(*b*). The Nusselt number drops by a factor 3 in figure 1(*c*) while the turbulent kinetic energy decays by almost one order of magnitude during the first stage of the transient. At the end of the initial transient, it appears that the flow becomes approximately laminar. However, since the Richardson number, $Ri_\tau \simeq 27$, at the end of the initial transient is much smaller than the critical value required for stability ((3.12) implies that, if $Ri_\tau < 881$, stratified channel flow with $Re_\tau = 180$ is linearly unstable), the flow cannot remain laminar and eventually must undergo a transition to turbulence. In the case of unstratified plane Poiseuille flow, the critical centreline Reynolds number based on linear analysis is equal to 5772, though, with finite-amplitude initial disturbances, subcritical transition has been observed for Re_c as low as 1000 (see Kleiser & Zang 1991 for an exhaustive review). In our simulation, a transition to turbulence occurs when $Re_c \simeq 4800$ at $tu_\tau/h \sim 9$. During transition, both the wall stress and the Nusselt number increase sharply. After transition, the flow tends toward a new turbulent, steady-state condition with overall transport coefficients that are smaller than the initial values corresponding to unstratified, fully developed channel flow. In fact, figure 1 shows that when $tu_\tau/h > 24$ the bulk quantities settle down around steady-state values of $Re_\tau \simeq 180$ and bulk Reynolds number $Re_b \simeq 3670$.

GFMK show the evolution of flow rate in figure 2 of Garg *et al.* (2000). The cases with $Ri_\tau = 45$ and 60, unlike the cases with lower values of Ri_τ, do not show convergence to a constant flow rate. Similarly, their figure 21(*a*) shows a plateau at $Re_\tau \simeq 90$ starting at $tu_\tau/h = 4$ and continuing up to the end of their simulation, $tu_\tau/h = 10$, without convergence to the theoretically expected result at steady state, namely the initial value of $Re_\tau \simeq 180$. Thus, probably due to the large computational efforts required, the authors did not continue their simulations long enough to obtain steady-state conditions, either laminar or turbulent. Indeed, our simulations also show a plateau in Re_τ during the transient ($4 < tu_\tau/h < 10$) as shown in figure 1(*a*); however, this plateau is followed by transition to a new balanced state with $Re_\tau \simeq 180$ along with reduced density transport at the wall as shown by the reduced Nusselt number. Such a transition to turbulence is expected based on our discussion of the analysis of Gage & Reid (1968) in § 3.4.

The stabilizing effect of stratification in the final, balanced state is linked to the reduced value of Nu, signifying inhibited density transport at the wall, the reduced value of wall skin friction, $c_f = 2u_\tau^2/u_b^2$, as well as the reduced value of normalized turbulent kinetic energy, K/u_b^2. The profiles in figure 2 show the relaminarization during the initial transient in more detail. Turbulent transport is almost completely suppressed as depicted in figure 2: the mean shear at the wall reduces and the velocity profile tends to assume a parabolic shape (figure 2*a*), the density gradient at the wall decreases and the density profile becomes flatter (figure 2*b*) (in the limit of the laminar regime it would be linear). During this initial period, the vertical turbulent fluctuations as well as the density fluctuations tend to vanish near the wall; however, they remain large in the core of the channel (figure 2*c, d*). These large values of the density and vertical velocity fluctuations in the core of the channel do not correspond to classical turbulence in figure 2(*e*), the buoyancy flux is countergradient in the outer region, $0.5 < z/h < 1$, at $tu_\tau/h = 1.15$, indicating transfer of energy from the density fluctuation to the vertical velocity fluctuation, and becomes vanishingly small at later time. Similarly, as shown in figure 2(*f*), the Reynolds shear stress, after transient

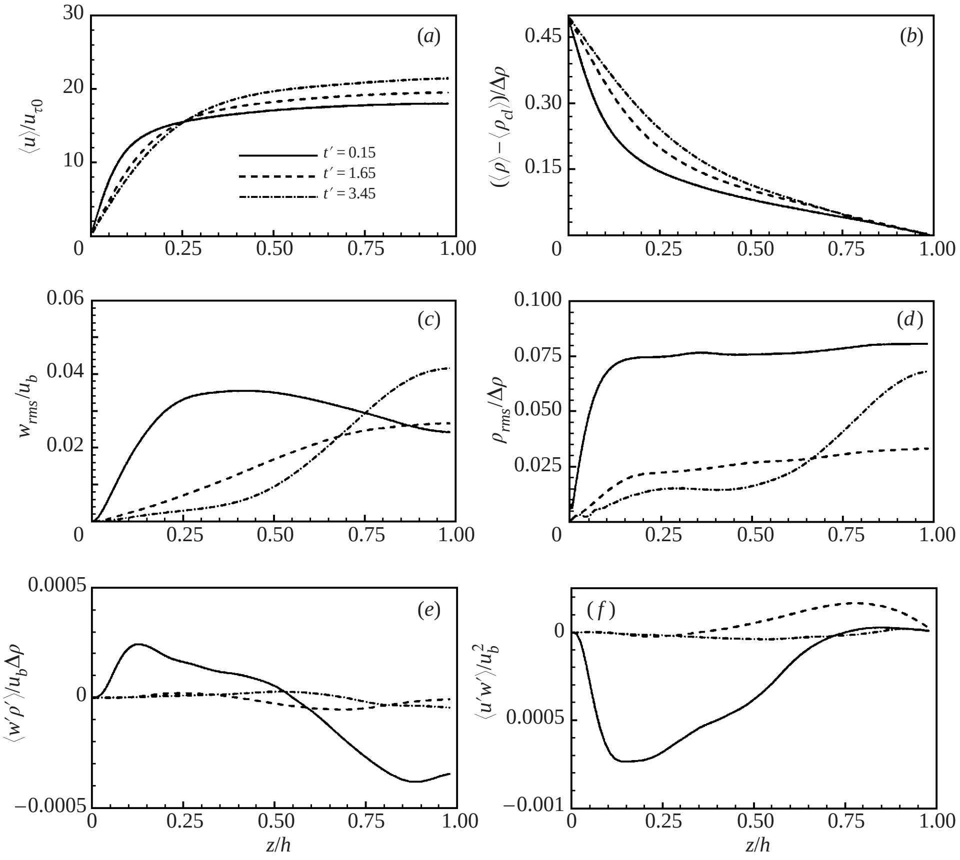

FIGURE 2. Plane averaged profiles at three different non-dimensional times ($t' = tu_\tau/h < 3.5$) during initial transient: (*a*) mean velocity; (*b*) mean density; (*c*) vertical turbulence level; (*d*) density r.m.s.; (*e*) vertical density flux; (*f*) Reynolds stress $\langle u'w' \rangle$.

countergradient values in the core of the channel, also becomes vanishingly small at $tu_\tau/h = 3.45$.

The transfer of potential energy to vertical kinetic energy followed by an almost zero value of the plane-averaged buoyancy flux during the initial transient suggests the presence of internal waves. Figure 3 shows visualizations of the flow field during the relaminarization process ($tu_\tau/h = 1.65$). The isopycnal surfaces and contours in figure 3(*a, b*) clearly show a strong wave system in the core of the channel, whereas, in the inner layer, the vertical undulations are suppressed. Vertical velocity fluctuations shown in figure 3(*c*) correspond to the same vertical section of the channel for which isopycnal contours are displayed in figure 3(*b*). A closer view of figure 3(*b, c*) shows that the upward excursions of the isopycnal surfaces correspond to positive vertical velocity (solid contours in figure 3*c*), whereas in the wave troughs the vertical velocity is negative (dashed contours in figure 3*c*) thus indicating a wave-like behaviour associated with the exchange of potential and vertical kinetic energy.

To summarize, there is buoyancy domination for all the cases studied here with $Ri_\tau \geqslant 60$ evidenced by relaminarization, as stated by GFMK, but the relaminarization is limited to the transient evolution of the flow. This complete suppression of turbulence during the initial transient is associated with internal waves set up in the core

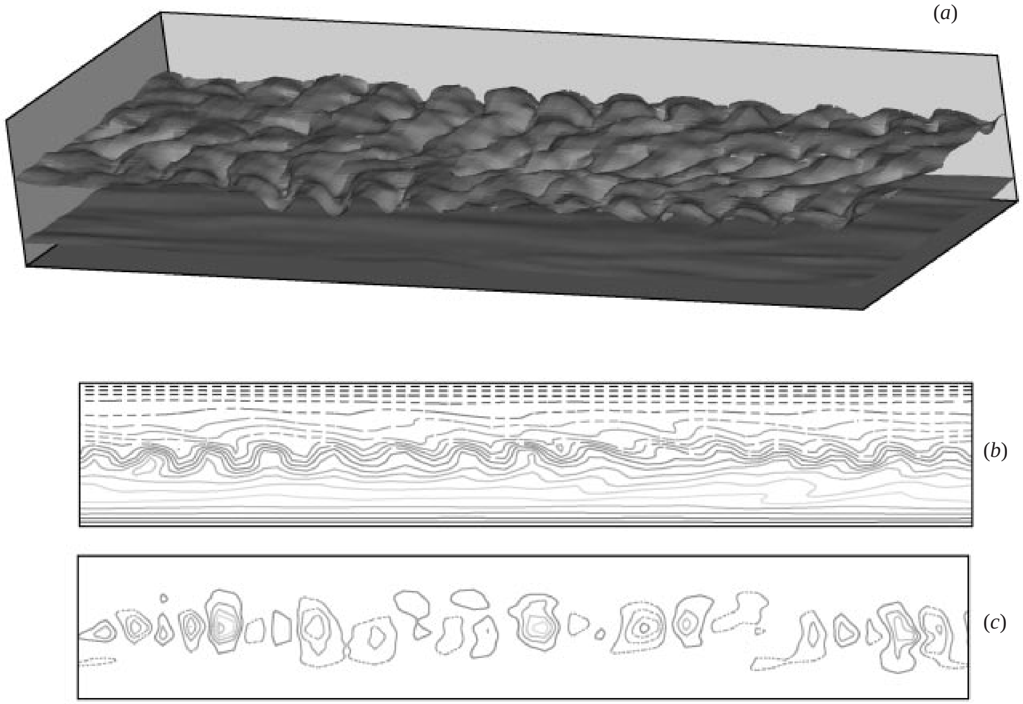

FIGURE 3. Visualization of flow field at $tu_\tau/h = 1.65$ during initial transient: (*a*) density iso-surfaces in the core of the channel and in the inner layer; (*b*) density isocontours in a vertical section of the channel; (*c*) vertical velocity isocontours corresponding to the section shown in (*b*).

of the channel that exchange the available potential energy with kinetic energy. These waves interfere with the turbulence maintenance mechanism at the wall as stated by GFMK. Later in time, these internal waves subside due to viscous dissipation and the wall region recovers, resulting in transition to turbulence. This equilibrium is a new buoyancy-affected state of turbulence, characterized by reduced skin friction, Nusselt number and buoyancy flux.

4.2. *Low-Richardson-number case*

The transient evolution in case C1 which has $Ri_\tau = 18$ and passive-scalar initial conditions is reported here. This case belongs to the buoyancy-affected regime of GFMK. Similar to case C2 discussed previously, turbulence is suppressed in the inner-layer, resulting in the reduction of the wall shear stress as well as the turbulent kinetic energy. However, an important difference with respect to the behaviour at higher values of Richardson number is that, in this case, stratification is not large enough for turbulence to be completely suppressed. In particular, figure 4(*d*) shows that the turbulent kinetic energy decreases by a small amount during the initial transient, in contrast to an order of magnitude decrease in case C2 during the initial phase of turbulence suppression. Later the flow is re-energized and a new turbulent condition is reached. Inspection of the Reynolds stress (not shown) as well as the vertical density flux (not shown) shows that turbulence is active during the transient. Unlike the previously discussed higher Richardson number cases, countergradient momentum and buoyancy fluxes in the core of the channel are absent when $Ri_\tau = 18$.

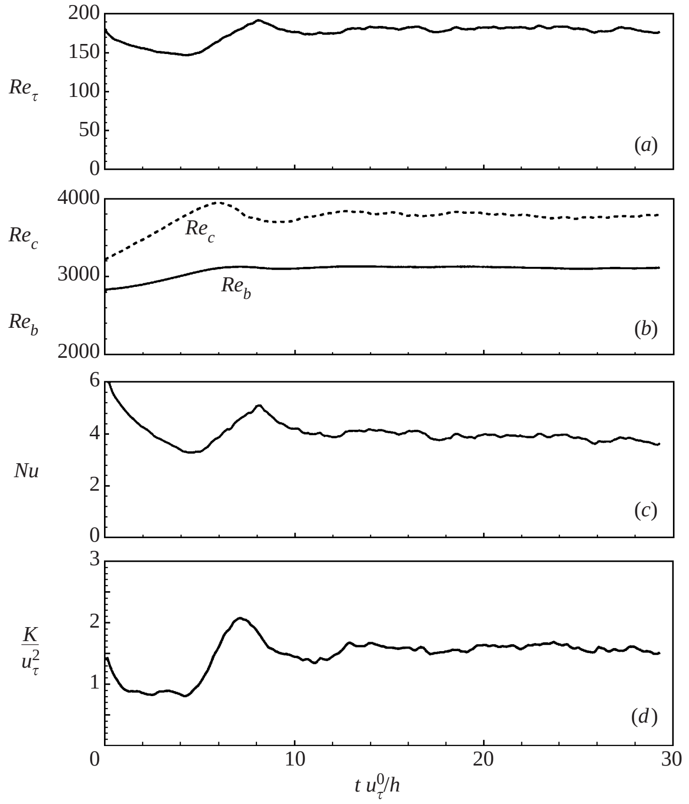

FIGURE 4. Time evolution of some bulk quantities for $Ri_\tau = 18$, starting from the passive scalar case: (*a*) friction Reynolds number; (*b*) bulk and centreline Reynolds numbers; (*c*) Nusselt number; (*d*) turbulent kinetic energy.

5. Buoyancy effects on the steady state

We have observed in the previous section that temporary relaminarization may occur during the initial transient, but a non-laminar regime with a statistical steady state is eventually reached. In this section, we discuss how stable stratification affects the flow and mixing characteristics of this new asymptotic regime. The cases examined span a wide range of Richardson numbers and table 1 lists relevant overall quantities for these cases. The statistics were obtained by time-averaging the horizontal plane averages, after the asymptotic regime is reached, over a sufficiently long time window, $tu_\tau/h \simeq 10$, to obtain converged values. In particular, we have checked that, in all cases, the sum of the viscous and the turbulent (resolved + SGS) shear stresses is a linear function of the wall-normal coordinate.

In Appendix C, the effects of different initialization procedures for the density field, inferred from additional simulations, is reported. The primary result is that the asymptotic state is independent of these initialization procedures.

5.1. *Mean velocity and density profiles*

Due to the effect of stable stratification, vertical momentum transport is suppressed with respect to the passive scalar case. Since the driving pressure gradient is constant, the viscous wall stress and, therefore, the slope of the mean velocity profile at the wall is invariant between cases as shown in figure 5. The reduced vertical momentum

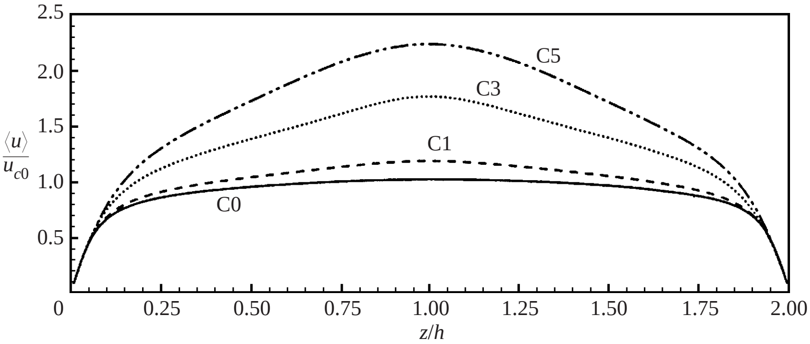

FIGURE 5. Mean velocity profile in global units, scaled with the centreline velocity of the passive scalar case, for several levels of stratification. Both halves of the channel are shown. Cases C0, C1, C3, C5 correspond to $Ri_b = 0$, 0.032, 0.112, 0.297, respectively.

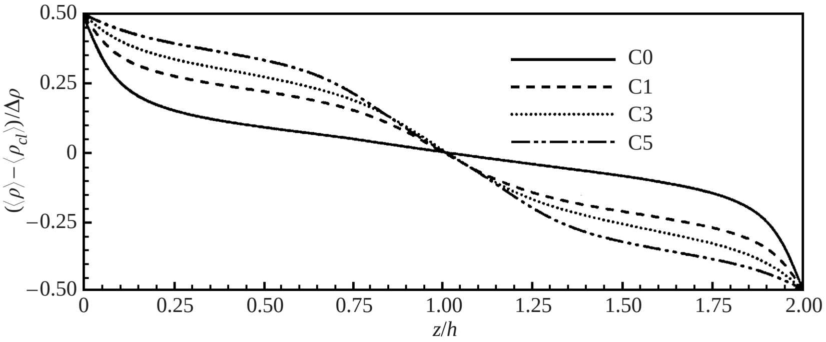

FIGURE 6. Mean density profile in global units for several levels of stratification. Both halves of the channel are shown.

transport with increasing stratification is manifested as the change in the mean velocity in the core region from a flat, well-mixed profile to a curved profile which, in the limit of relaminarization, would be parabolic. The centreline velocity increases systematically with stratification in figure 5 and so does the centreline Reynolds number and bulk Reynolds number in table 1. The friction coefficient, c_f, and the Nusselt number, Nu, are also shown in table 1. In accord with previous investigations by KUOM and GFMK, stable stratification leads to a systematic reduction in both Nusselt number and friction coefficient. Since the simulations are performed with constant mean streamwise pressure gradient (therefore, constant friction velocity at steady state) the reduction of the friction coefficient is due to the increased bulk velocity of the flow.

The mean density profile is also affected by stratification (figure 6). In particular, the increase of the Richardson number introduces two main changes with respect to the passive scalar case. First, it reduces the density gradient at the wall (and consequently the Nusselt number, in table 1). Second, the density profile becomes sharper in the core of the channel indicating a tendency to form a density interface. Note that, in the limit of complete relaminarization, the mean density variation would be a straight line between the fixed values of the density at $z/h = 0$ (bottom wall) and $z/h = 2$ (top wall). Although, the slope of the density profile at the wall decreases with increasing bulk stratification and tends to that of the laminar profile, the slope at the core of

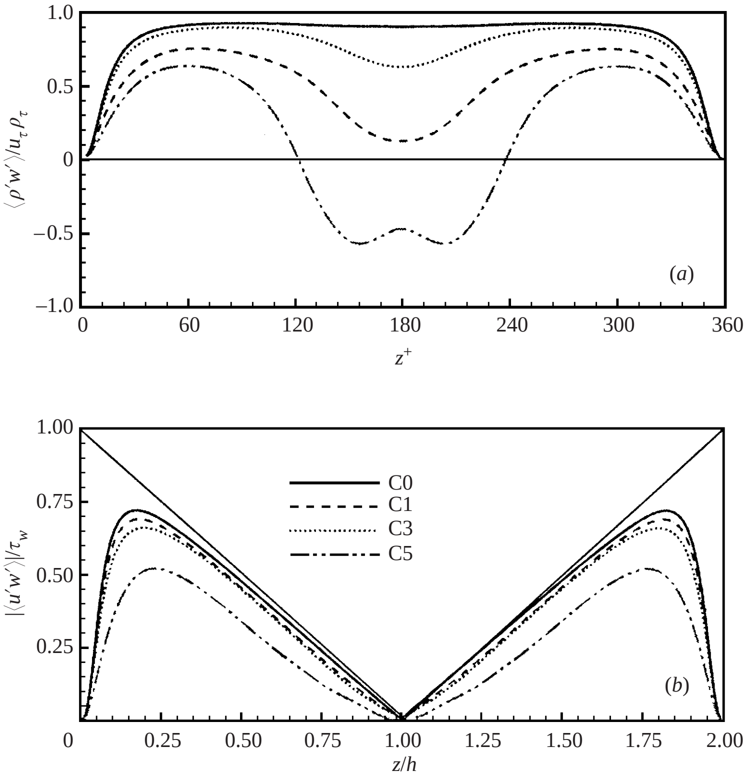

FIGURE 7. The influence of stratification on (*a*) buoyancy flux, and (*b*) momentum flux. The plotted flux is the sum of resolved and subgrid model components. Cases C0, C1, C3, C5 correspond to $Ri_b = 0$, 0.032, 0.112, 0.297, respectively.

the channel increases and does not tend towards the laminar value. For cases C1–C5 the magnitude of the mean density gradient initially decreases away from the wall as expected of turbulent mixing and then increases when the core of the channel is approached.

Such a non-monotone behaviour of the mean density gradient can be explained by considering the Reynolds-averaged density equation which, in channel flow, reduces to

$$\langle\rho'w'\rangle(z) - k\frac{\partial\rho(z)}{\partial z} = \text{constant}, \tag{5.1}$$

where the constant is the wall value of the molecular flux, $-k(\partial\rho/\partial z)_w$. Using the friction density, ρ_τ defined by (3.1), we rewrite (5.1) as follows:

$$-\frac{\partial\rho}{\partial z} = -\left(\frac{\partial\rho}{\partial z}\right)_w \left(1 - \frac{\langle\rho'w'\rangle}{\rho_\tau u_\tau}\right). \tag{5.2}$$

The last term in (5.2) is the buoyancy flux (henceforth used interchangeably with the mass flux) normalized using inner variables, and its variation is shown in figure 7(*a*). In the passive scalar case, $Ri_b = 0$, the normalized buoyancy flux is almost unity away from the wall, $z/h > 0.1$; this corresponds to the 'constant flux' hypothesis of neutral boundary layers. However, its value departs from unity significantly at higher values of Ri_b. In the stratified cases, the buoyancy flux first increases away from the wall and then decreases in the core of the channel. Correspondingly, according

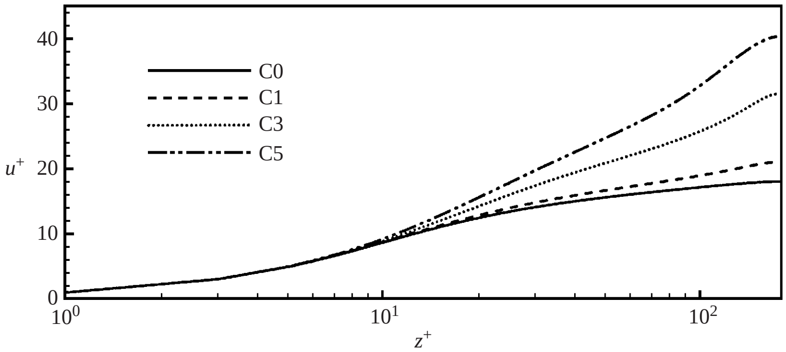

FIGURE 8. Mean velocity profile in wall units for several levels of stratification. Cases C0, C1, C3, C5 correspond to $Ri_b = 0$, 0.032, 0.112, 0.297, respectively.

to (5.2), the magnitude of the mean density gradient decreases and then increases as observed in figure 6. In case C5, according to (5.2) the observed countergradient transport, i.e. negative values of the buoyancy flux, would lead to a local mean density gradient which is larger in magnitude than the wall value, as indeed observed for the corresponding density profile in figure 6. To summarize, the mean density profiles show non-monotone behaviour of density gradient and, even for large overall stratification, there are local regions which are mixed by boundary-layer turbulence.

The variation of turbulent momentum flux is shown in figure 7(*b*). The maximum value decreases with increasing stratification, with an especially large decrease between cases C3 and C5. Note that the sum of turbulent flux and viscous flux is equal to the straight line in the figure. Case C5 shows that the viscous contribution in the core of the channel becomes increasingly important in strongly stable flows.

The LES result of sharpened density profiles in the presence of increasing overall stratification has been also observed in other laboratory and field studies of mixing in stably stratified flows. The density mixing in stratified channel flow can be conceptualized as that between two turbulent regions (upper and lower near-wall regions) subject to an overall stable density difference. It is instructive to look at density structure in flows with a similar configuration. For example, Moore & Long (1971) investigated the stably stratified shear flow between two counterflowing turbulent layers set up by injection of approximately horizontal jets with a salinity contrast at the upper and lower boundaries of a tank. The authors find that there is a steady-state vertical density structure that consists of upper and lower regions, almost uniformly mixed by turbulence, separated by a central region where most of the density variation occurs. Crapper & Linden (1974) studied the central region between two layers stirred by a horizontal grid and found that, with increasing stable stratification, the density profile sharpens in the central region and, under some circumstances, a steady density interface is possible. It appears that the sharpening of the density profiles observed in our channel flow LES is consistent with other observations in similar stratified mixing situations.

The mean profiles, plotted in wall units, as a function of the coordinate $z^+ = u_\tau z/\nu$ are now discussed. The mean velocity profiles for the different cases are shown in figure 8. In the unstratified case, three zones can be identified: the inner region ($z^+ < 30$), the logarithmic region ($30 < z^+ < 150$) where the mean velocity variation is approximately linear in log-linear coordinates, and a small core region for $150 < z^+ < 180$ where there is a deviation from the log law. The classical expression for the

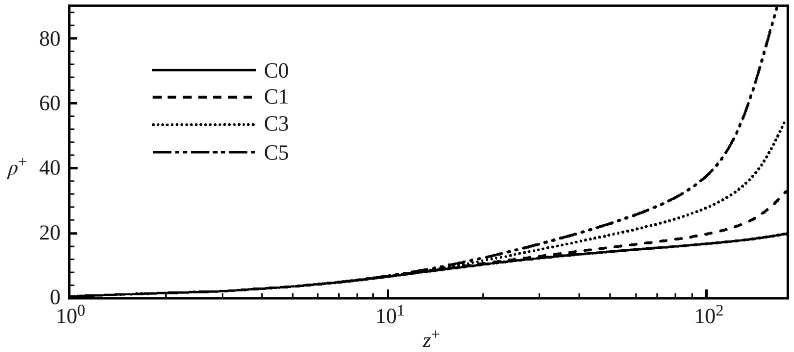

FIGURE 9. Mean density profile in wall units for several levels of stratification. Cases C0, C1, C3, C5 correspond to $Ri_b = 0$, 0.032, 0.112, 0.297, respectively.

law of the wall in the neutral case is

$$u^+ = A \ln z^+ + B.$$

Stable stratification increases the slope, A, of the log-zone and reduces the intercept, B, of the velocity profile. Also, the core region appears to be widened and characterized by a larger mean velocity gradient compared to the passive scalar case. The density profiles plotted using wall units in figure 9 show that, similar to the mean velocity profile, there are three zones. Under strongly stable stratification, the vertical extent of the log-zone is progressively reduced while the core region widens.

5.2. *Turbulence level and anisotropy*

The streamwise intensity is reduced in most of the channel with respect to the passive scalar case, figure 10(a). The wall-normal turbulent intensity shown in figure 10(b) behaves differently depending on the level of stratification. For weakly stratified flow (cases C1, C2 and C3) it is reduced throughout the channel. In the other cases, the reduction of vertical fluctuations in the wall layer and log-zone with increasing Ri continues; however, the fluctuations are enhanced in the core region. When stratification increases, countergradient density fluxes are observed in the core region (see figure 7), that act as a source term in the $\langle w'w' \rangle$ transport equation. The spanwise velocity fluctuations shown in figure 10(c) decrease with increasing stratification, except for case C5. The density fluctuations in the log-zone decrease consistently with Ri_b. However, ρ_{rms} in the core of the channel increases with increasing Ri_b.

The ratio between the vertical and the streamwise intensity is shown in figure 11. The magnitude near the wall, $0 < z^+ < 30$, is nearly unchanged among cases indicating that, in this zone, the structural characteristics of turbulence are not affected by stratification. In contrast, a strong decrease with increasing Ri_g is evident in the log zone, showing that, in this zone, stratification preferentially diminishes the transfer of energy from streamwise to vertical velocity fluctuations. Near the centreline, vertical velocity fluctuations increase to a magnitude closer to that of the streamwise component. The Reynolds shear stress (see figure 7) is strongly reduced by stable stratification as well, suggesting that the sweep–ejection events known to be critical to maintain wall-bounded turbulence are modified.

The state of anisotropy of the Reynolds stresses can be shown using the Lumley invariant map. The quantities $II_b = b_{ij}b_{ji}$ and $III_b = b_{ij}b_{jk}b_{ki}$ are two non-zero invariants of the anisotropy tensor, $b_{ij} = \langle u'_i u'_j \rangle / 2K - \delta_{ij}/3$; the other invariant, the

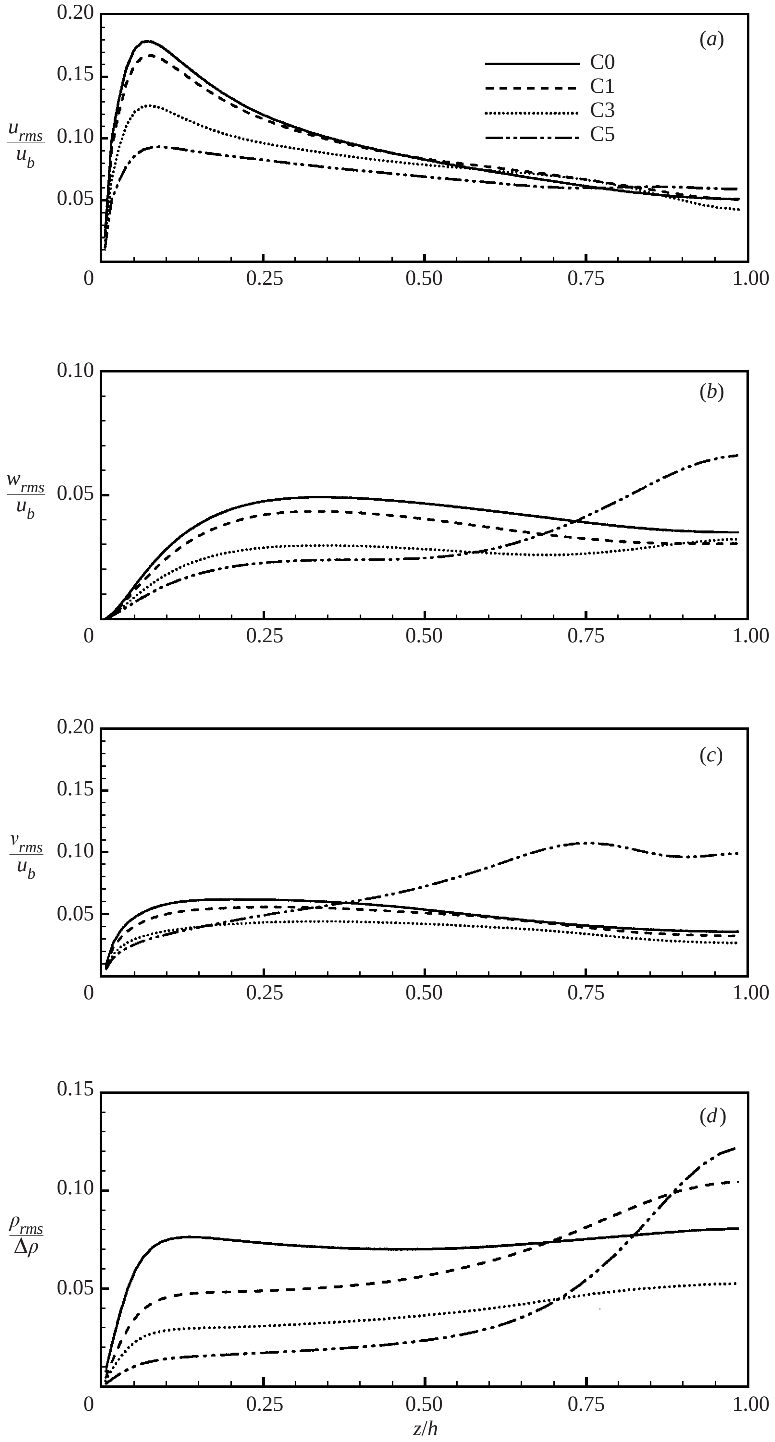

FIGURE 10. Turbulence statistics in global units for several levels of stratification: (*a*) streamwise velocity, (*b*) vertical velocity, (*c*) spanwise velocity, and (*d*) density. Cases C0, C1, C3, C5 correspond to $Ri_b = 0$, 0.032, 0.112, 0.297, respectively.

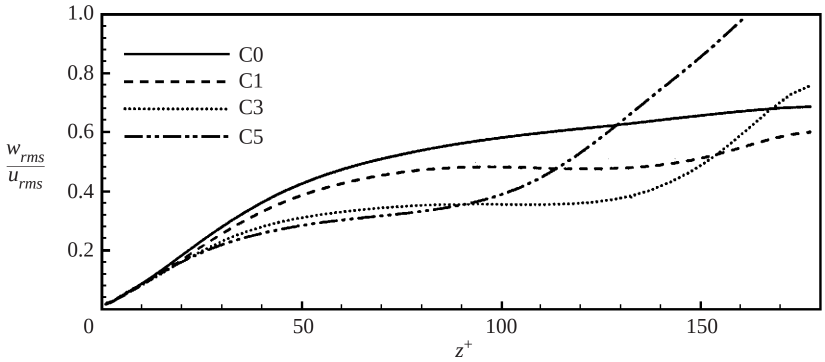

FIGURE 11. The ratio of vertical and streamwise Reynolds stresses for several levels of stratification.

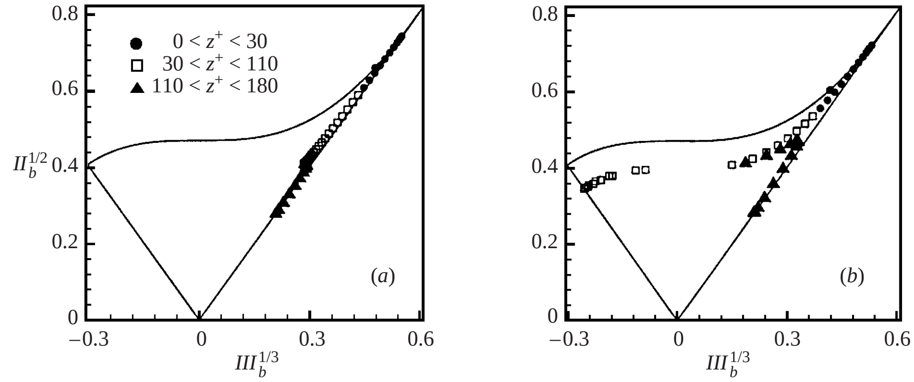

FIGURE 12. The Reynolds stress anisotropy shown using the Lumley invariant map: (*a*) weakly stratified case C1 with $Ri_b = 0.032$, and (*b*) strongly stratified case C5 with $Ri_b = 0.297$.

trace, is identically zero. The quantity, $II_b^{1/2}$ quantifies the magnitude of the anisotropy, while the 'shape' of the anisotropy can be quantified by the corresponding value of $(II_b^{1/2}, III_b^{1/3})$. All realizable states of fluctuating motion are constrained to lie within the 'triangular' region shown in figure 12. The linear sides originating from the origin (the point of isotropy) represent axisymmetric turbulence. The right-hand side of the 'triangle' with $III_b > 0$ represents cigar-shaped turbulence with two eigenvalues of the Reynolds stress tensor smaller than the third, while the left-hand side with $III_b < 0$ represents pancake-shaped turbulence with two eigenvalues larger than the third. The upper curve of the 'triangle' corresponds to two-component turbulence where one of the eigenvalues is identically zero. Figures 12(*a*) and 12(*b*) contrast the state of anisotropy between the low-*Ri* case C1 and the high-*Ri* case C5. In general, the magnitude of the anisotropy, II_b, decreases with distance from the wall. In both cases, the fluctuating motion is two-component at $z^+ = 1$ because the wall-normal component is much smaller than the other components. The motion relaxes to a cigar-shaped axisymmetric state (essentially because u_{rms} is larger than $v_{rms} \simeq w_{rms}$) in the region $z^+ < 30$. In the region $30 < z^+ < 110$ there is substantial difference between the two cases: the high-*Ri* case shows a change towards pancaked-shaped turbulence (the left-hand side of the 'triangle' with $III_b < 0$) with increasing z^+, while the low-*Ri* case continues to stay near the right-hand side. The implication is that, in the presence of stable stratification, the fluctuating motion is more horizontal,

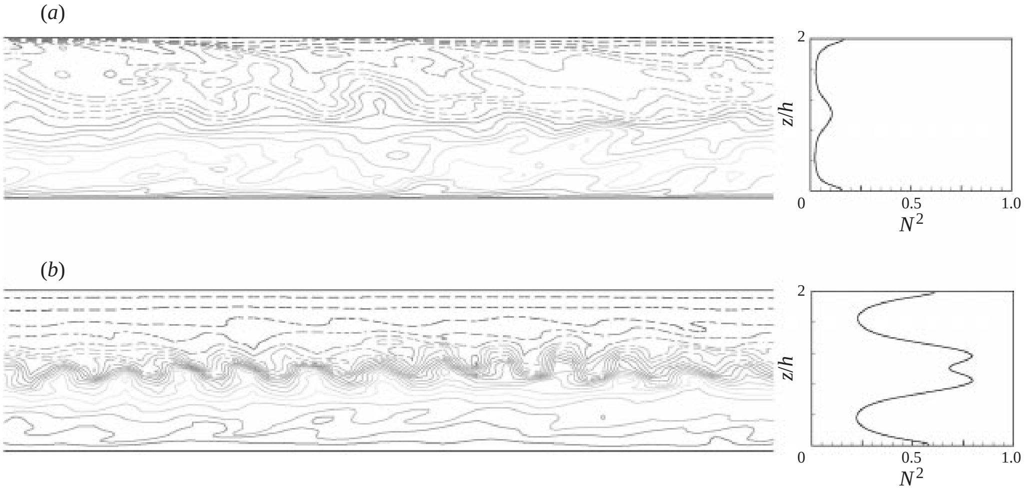

FIGURE 13. Isopycnals in a vertical cut across the whole channel after statistical steady state is achieved: (*a*) moderate stable stratification (C2) ($tu_\tau/h = 20$); (*b*) strong stable stratification (C5) ($tu_\tau/h = 20$).

with the vertical component smaller than the horizontal components. However, the fluctuating motion is not strictly two-component. The behaviour in the core region, $110 < z^+ < 180$, is similar between the two cases in that the Reynolds stresses relax towards isotropy because the mean shear decreases.

Stable stratification also reduces the vertical buoyancy flux when the Richardson number increases (figure 7*a*). In agreement with the data of KUOM, in the case of strong stratification, the core of the channel is increasingly characterized by the presence of countergradient density fluxes. Note that the unnormalized value of the buoyancy flux decreases more dramatically than that suggested by figure 7(*a*) because ρ_τ decreases with increasing Ri_b. Similarly to the turbulent intensities, the ratio of the vertical and streamwise density fluxes (not shown) is mainly affected away from the wall. The vertical buoyancy flux is preferentially damped relative to the streamwise flux.

5.3. *Visualizations of the instantaneous fields*

Figure 13 shows isopycnals, that is isocontours of the instantaneous density field, in the fully developed regime, for two different cases, C2 and C5.

It is clear that turbulence and internal waves coexist. Specifically, figure 13(*a*) shows that, for moderately stratified flow (C2), waves are present in a narrow region around the channel centreline, whereas the region near the wall has intermittent ‘bursts’ associated with near-wall turbulence. The square of the Brunt–Väisälä frequency N^2 (reported on the right-hand side of figure 13*a*) rapidly decreases in the wall layer and is nearly constant in the core of the channel apart from a narrow area at the centre where wave activity is observed.

On the other hand, in the strongly stratified case C5 (figure 13*b*) the waves extend into the near-wall region. In this case, after the rapid decrease from its wall value, N^2 reaches a local minimum and then again increases in a wide part of the channel. Such an increase is related to the previously discussed sharpening of the mean density profile in the core of the channel. We have also plotted the turbulent streaks at $z^+ \simeq 12$ for three different cases, namely neutral flow, and two stratified cases, C2

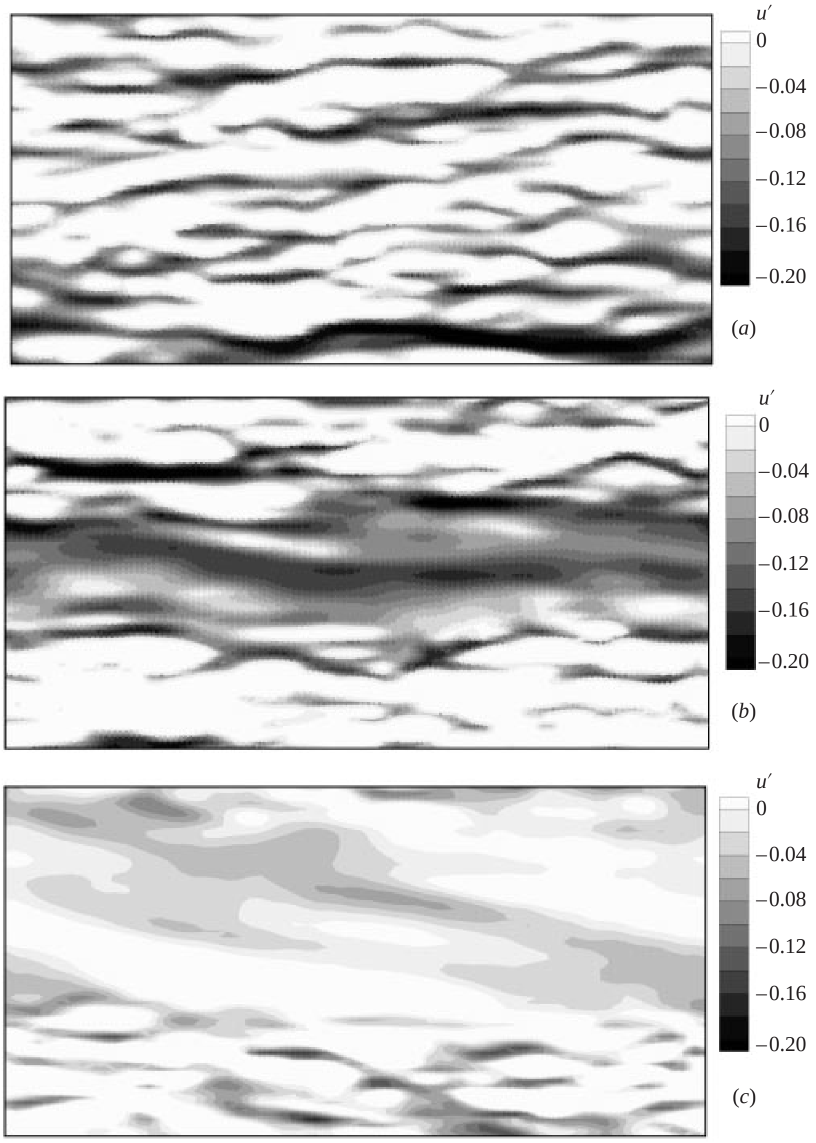

FIGURE 14. Low-speed streaks at $z^+ \simeq 12$: (*a*) neutral flow ($tu_\tau/h = 20$); (*b*) moderate stable stratification (C2) ($tu_\tau/h = 20$); (*c*) strong stable stratification (C5) ($tu_\tau/h = 20$). Here u' is the fluctuation with respect to the plane-averaged velocity and, thus, regions with velocity lower than the plane-averaged velocity are displayed in various shades of grey.

and C5, in figure 14. Narrow and elongated low-speed streaks are present in the neutral case (figure 14*a*) signifying flow ejections from the wall that cause mass and momentum to mix. In the case C2, the structures are less energetic but still present in the flow (figure 14*b*). Finally, the visualization, figure 14(*c*), corresponding to the case of strong stratification (C5) is remarkably different. There is no evidence of coherent low-speed streaks, and, furthermore, the magnitude (see the contour level bar) is much smaller than that in the previous cases. The absence of coherent structures is the signature of the strong suppression of vertical transport of mass and momentum.

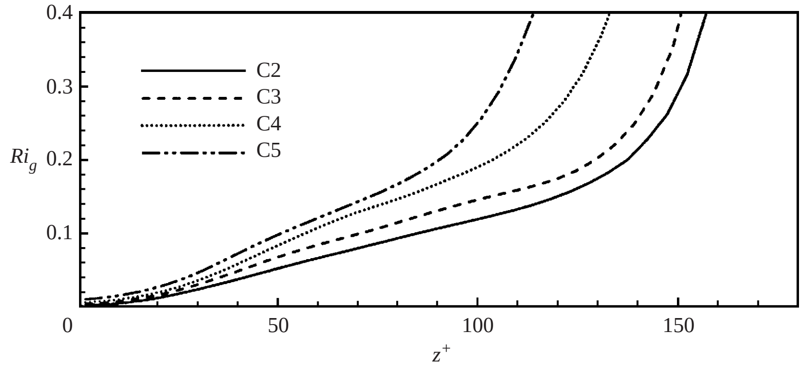

FIGURE 15. Gradient Richardson number as a function of the vertical coordinate for different cases. Cases C2, C3, C4, C5 correspond to $Ri_b = 0.0685, 0.112, 0.188, 0.297$, respectively.

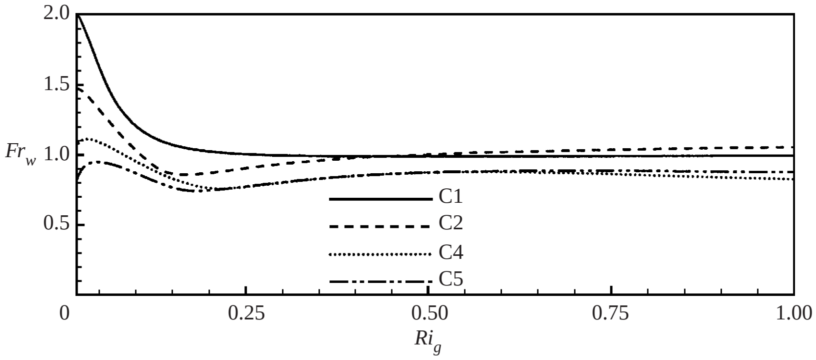

FIGURE 16. Vertical Froude number versus gradient Richardson number for different friction Richardson numbers.

5.4. *The gradient Richardson number*

Profiles of the local value of the gradient Richardson number, $Ri_g = N^2/S^2$, are shown in figure 15. The gradient Richardson number is singular at the centreline and is very large in a narrow region near the centreline. On the other hand, in a large region from the wall onwards, Ri_g ranges between 0.02 and 0.2 and is well-behaved. There is an equilibrium region where the variation of Ri_g is linear as suggested by (3.7). For a given case, Ri_g exhibits monotone increase from the wall towards the centre of the channel. Also, cases with increasing Ri_τ have larger values of Ri_g at the same distance from the wall. It is remarkable that the value $Ri_g \simeq 0.2$ seems to be the value that determines the point for the abrupt change of the slope of the $Ri_g(z)$ profile.

The vertical Froude number,

$$Fr_w = w_{rms}/NL_e,$$

with

$$L_e = \rho_{rms}/(\partial\langle\rho\rangle/\partial z)$$

denoting the Ellison scale, is plotted as a function of the gradient Richardson number for four cases in figure 16. For a given case, it appears that in the region with $Ri_g < 0.20$ the Froude number decreases somewhat, showing that the vertical buoyancy force becomes increasingly important in the vertical momentum balance. The decrease of

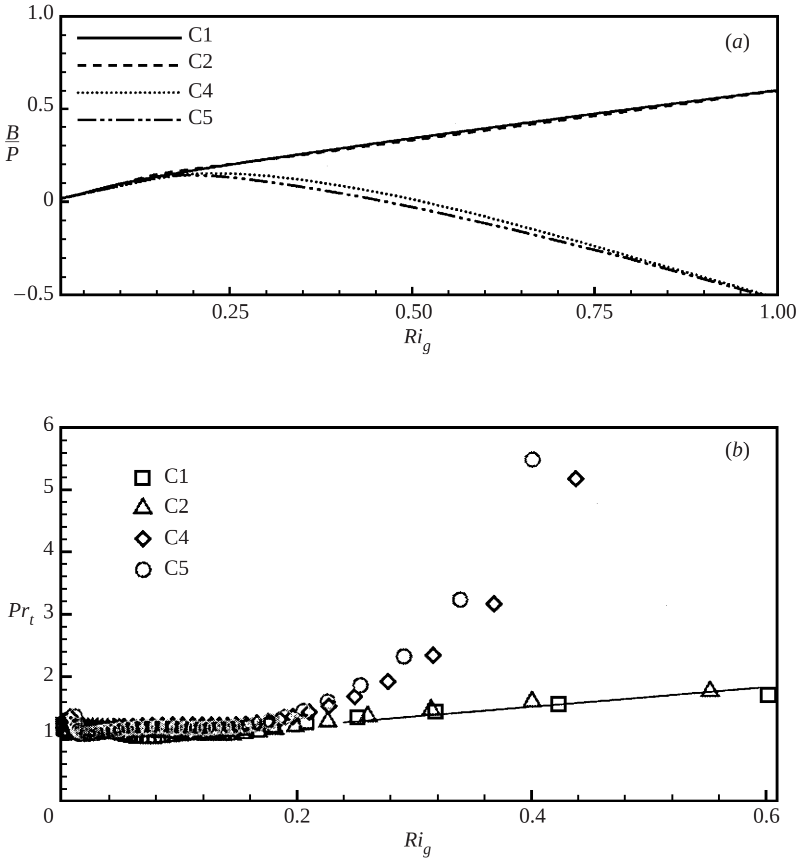

FIGURE 17. The influence of gradient Richardson number on (*a*) the ratio, B/P (a surrogate for mixing efficiency), and (*b*) the turbulent Prandtl number, Pr_t. Cases C1, C2, C4, C5 correspond to $Ri_b = 0.032, 0.0685, 0.188, 0.297$, respectively.

Froude number with increasing Richardson number is to be expected. Nevertheless, it is interesting to note that, in agreement with previous analysis of Sarkar (2000), Fr_w asymptotes to an $O(1)$ constant at large values of Ri_g. In channel flow $Fr_w \rightarrow 0.8$, while $Fr_w \rightarrow 0.6, 0.75$ in uniformly sheared flow.

The ratio $B/P = Ri_f$, the flux Richardson number, or sometimes, B/ϵ, is often used to represent mixing efficiency. Here, $B = -(g/\rho_0)\langle\rho' w'\rangle$ is the buoyancy flux while $P = -(\partial\langle\bar{u}\rangle/\partial z)\langle u'w'\rangle$ is the production of turbulent kinetic energy. Note that, within the framework of the eddy viscosity hypothesis,

$$\langle u'w'\rangle = -D_u \frac{\partial\langle u\rangle}{\partial z}, \tag{5.3}$$

$$\langle\rho' w'\rangle = -D_\rho \frac{\partial\langle\rho\rangle}{\partial z}, \tag{5.4}$$

the ratio

$$\frac{B/P}{Ri_g} = \frac{D_\rho}{D_u} = \frac{1}{Pr_t}, \tag{5.5}$$

where Pr_t is the turbulent Prandtl number.

The behaviour of the ratio B/P and turbulent Prandtl number, Pr_t, for several levels of stratification and along the vertical direction is worth describing in some details (figure 17) as follows.

(*a*) For $0 < Ri_g < 0.2$, the value of B/P increases linearly with the gradient Richardson number in all the cases investigated. Correspondingly, the turbulent Prandtl number is nearly equal to 1 in the neutral case and it slightly increases with increasing Ri_g. The value of $Pr_t \simeq 1$ observed here is consistent with previous studies of neutral flows where values of turbulent Prandtl number in the range of $0.7 < Pr_t < 1.2$ have been measured depending on the specifics of the flow. Furthermore, previous laboratory and numerical studies of stratified uniform shear flow, Gerz *et al.* (1989) and Jacobitz *et al.* (1997), show that Pr_t increases little in the range $0 < Ri_g < 0.2$ just as in the current study.

(*b*) For $Ri_g > 0.2$ the behaviour is qualitatively different, depending on the level of stratification. For weak stratification, cases C1 and C2, the value of B/P continues to increase with Ri_g but at a smaller rate and, thus, the value of Pr_t increases somewhat with increasing Ri_g. For stronger stratification, cases C4 and C5, after attaining a maximum value (approximately 0.14), B/P decreases with increasing Ri_g. Consequently, Pr_t increases rapidly. A more rapid increase of Pr_t for $Ri_g > 0.2$ has also been observed in previous laboratory and numerical studies of vertically sheared flow as summarized by Schumann & Gerz (1995), see their figure 3. The behaviour of Pr_t at large values of Ri_g is of interest in developing parameterizations of mixing. If the mixing efficiency, $B/P \rightarrow$ const, then, according to (5.5), Pr_t would increase linearly with Ri_g. However, reviews of data by Ivey & Imberger (1991) and Schumann & Gerz (1995) suggest that B/P eventually decreases with Ri_g. The strongly stratified cases C4 and C5 show a decrease of B/P when $Ri_g > 0.2$ and, consequently, a dramatic increase of Pr_t which is superlinear. However, cases C1 and C2 with weaker overall stratification show a more moderate and quasi-linear increase of Pr_t.

(*c*) Finally, in cases C4 and C5, when $Ri_g > 0.45$, countergradient buoyancy flux is observed so that B/P becomes negative. Countergradient buoyancy fluxes have observed previously, for example, by Gerz *et al.* (1989) and Holt *et al.* (1992) in uniform shear flow when a 'transition' Richardson number (between 0.4 and 0.7) is exceeded, and by KUOM in the experimental investigation of strongly stratified channel flow. Such behaviour with negative values of B/P is not representative of a turbulent Prandtl number, since the eddy viscosity concept ceases to hold.

6. Discussion and concluding remarks

A wide range of levels of stable stratification in turbulent channel flow is investigated by the LES technique. A mixed model with a dynamic eddy viscosity component and a scale-similar component is used. The eddy diffusivity coefficients for the subgrid momentum flux and buoyancy flux, instead of being prescribed, are calculated with a dynamic procedure.

Based on the results it appears that the increase of stable stratification induces remarkable changes in the characteristics of wall-bounded turbulence. Our results in the strongly stratified cases considered here are consistent with the experimental finding of KUOM that, in the case of strong stratification, active turbulence survives in the near-wall region and coexists with internal wave activity in the core of the channel. Turbulence levels, momentum and buoyancy fluxes are generally suppressed. The turbulent motion appears more horizontal (but not strictly two-component) with increasing Richardson number. Countergradient density fluxes in the core of the channel along with enhanced vertical velocity fluctuations are observed both in the

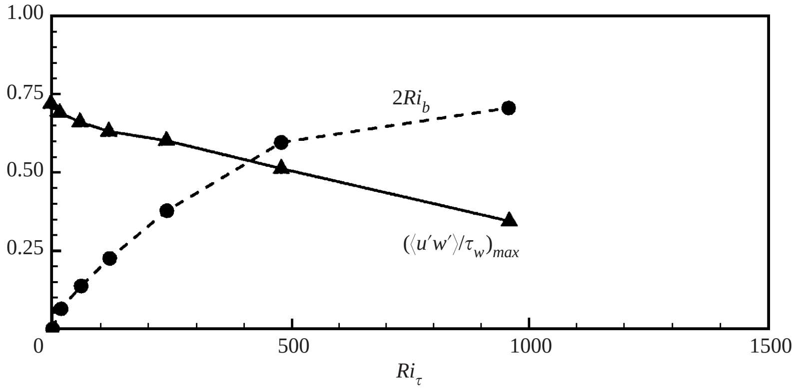

FIGURE 18. The variation of maximum turbulent shear stress in the channel and the behaviour of the bulk Richardson number in the various cases.

experiments of KUOM and in our simulations for sufficiently large stratification ($Ri_b = 0.112$, 0.188 and 0.297 in the LES). With increasing Richardson number, the buoyancy-affected region encroaches into the inner layer with active turbulence. At the highest stratification studied here, the coherent low-speed streaks near the wall associated with near-wall turbulence tend to be suppressed.

The final statistical state reached in channel flow in cases C1–C5 corresponds to active, but suppressed, turbulence near the wall and is not a laminar flow. This result is consistent with the theory of Gage & Reid (1968) which, when applied to channel flow at $Re_\tau = 180$, predicts that linearly evolving disturbances are unstable when $Ri_\tau < 881$, a condition met by the values of Ri_τ in all the cases simulated here. On the other hand, GFMK identify a buoyancy-dominated regime with relaminarization for $Ri_\tau > 45$. Our simulations show such relaminarization for cases C2–C5 but it occurs only for a limited period during the initial transient, and on continuing for a time longer than GFMK the flow recovers to a new asymptotic condition of stratified turbulence. The friction Reynolds number recovers to its initially imposed value as demanded by integral momentum conservation. The stratification imposed at $t = 0$ has an associated potential energy which, during the initial transient, is exchanged with kinetic energy (primarily that of the vertical component) through a strong internal wave system. Although effective in interfering with near-wall turbulence during the early evolution, the wave amplitude subsides later on in time, allowing near-wall turbulence to recover.

The highest stratification level reported in the main body of the text is $Ri_\tau = 480$. We performed another simulation with $Ri_\tau = 960$, a value larger than the critical value based on linear instability theory, $Ri_{\tau,crit} = 881$. The transient is highly oscillatory during the evolution of the bulk quantities; however, after a very long time, $tu_\tau/h \simeq 70$, an asymptotic state with average $Re_\tau = 180$ is reached. Figure 18 shows that, although the maximum value of the Reynolds shear stress in the channel consistently decreases with increasing stratification, indicating the suppression of turbulence, the asymptotic state for the case with $Ri_\tau = 960$ is still turbulent. Evidently, for turbulent initial conditions, after the initial 'relaminarization', there is subcritical transition in this case. Based on extrapolation of the trend shown in figure 18, the flow would probably relaminarize for sufficiently large stratification at the moderate Reynolds number of the current simulations. For high-Reynolds-number geophysical flows, relaminarization may be difficult to achieve in practice. According to linear theory,

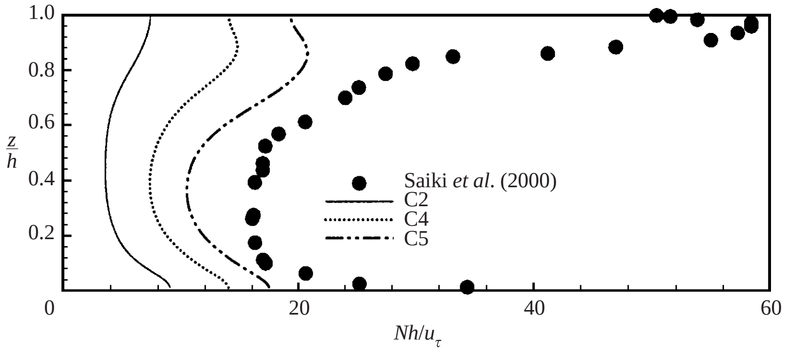

FIGURE 19. Profiles of the Brunt–Väisälä frequency. Lines are results from the current LES. Symbols correspond to the LES of Saiki *et al.* (2000) which, although at a significantly stronger stratification level and different Reynolds number, is given for qualitative comparison. Cases C2, C4, C5 correspond to $Ri_b = 0.137$, 0.188, 0.297 respectively.

$Ri_b > 0.5$ is the condition for stability of infinite-Reynolds-number Poiseuille flow. The variation of Ri_b shown in figure 18 shows that Ri_b increases rather slowly with increasing stratification when it is large.

The density field is mixed by boundary-layer turbulence in channel flow and is thus generally relevant to the vertical density structure in boundary-driven geophysical flows, for example the wind-driven upper ocean, the benthic boundary layer and the atmospheric boundary layer. We find that, with increasing overall stable stratification, the mean profile becomes significantly sharper in the core of the channel, see figure 6. Even at the largest stratification level, $Ri_b = 0.297$, the density profile is far from the linear, laminar profile connecting the fixed values at the upper and lower walls; the slope at the centreline is significantly larger than the laminar value. Our observation of sharpened density profiles in turbulent channel flow is reminiscent of local regions of enhanced density gradients that are often observed in the stably stratified ocean and atmosphere as discussed by Turner (1973). Mixing of the density field in turbulent channel flow can be idealized as a central region which is driven by two forced regions of turbulence at the top and bottom, respectively. Laboratory experiments by Moore & Long (1971) and Crapper & Linden (1974), which have a similar idealization of the mixing situation, also show the formation of thin regions with large density variation as observed in our LES of channel flow.

It is of interest to compare our LES results with those of recent studies of the stable atmospheric boundary layer. Saiki *et al.* (2000) studied the response of a neutral boundary layer to a cooling heat flux gradually applied to the surface. Their figure 9 shows a steady-state profile of N which, after normalization, is shown along with profiles from the current LES cases in figure 19. According to our LES results, with increasing stable stratification, N tends to develop a non-monotone behaviour, with a local maximum near the wall and another local maximum in the vicinity of the centreline. The results of Saiki *et al.* (2000), which correspond to a much larger stratification and Reynolds number than our cases, shows an even stronger non-monotone behaviour. Internal waves developing in the region between the top of the boundary layer (where the Reynolds shear stress goes to zero and $Ri_g \simeq 0.2$) and the top of the capping inversion are observed by Saiki *et al.* (2000). In the strongly stratified cases C4 and C5, we also find internal wave activity in the region between $Ri_g \simeq 0.2$ and the centre of the channel. Kosovic & Curry (2000) simulated the stable

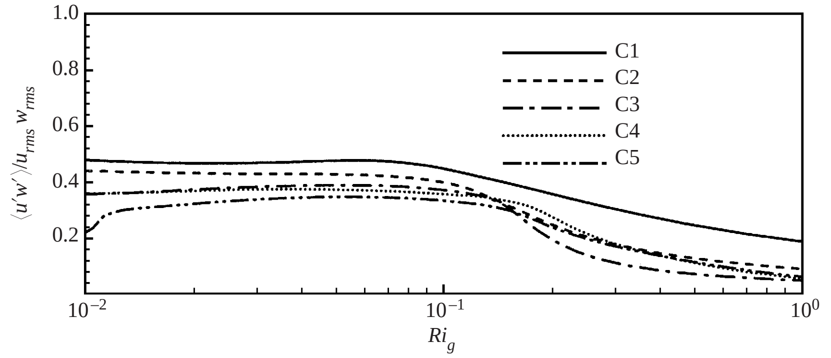

FIGURE 20. Correlation coefficient of the momentum flux as a function of the gradient Richardson number for several levels of stratification. Cases C1, C2, C3, C4, C5 correspond to $Ri_b = 0.032$, 0.0685, 0.112, 0.188, 0.297, respectively.

atmospheric boundary layer for a number of different conditions. All cases showed a turbulent boundary layer above which a region with internal wave activity was observed. To summarize, although the stably stratified atmospheric boundary layer has different boundary conditions with respect to stably stratified channel flow, both exhibit features generic to stably stratified wall-bounded flows.

There are at least three Richardson numbers that have been used by previous investigators: the friction Richardson number Ri_τ and the bulk Richardson number Ri_b are single numbers while the local gradient Richardson number, $Ri_g(z)$, is a function of the vertical coordinate. Since the flow is driven by a constant mean pressure gradient, at steady state, the final value of Ri_τ is the same as the initially imposed value making it convenient to distinguish between different cases. Nevertheless, it must be recognized that stratification affects both near-wall turbulence transport and that away from the wall and there is no reason to prefer Ri_τ over Ri_b.

As discussed in the introduction, the local value of the gradient Richardson number, Ri_g, is generally recognized as the important local parameter for describing stratification effects in shear flows without walls and to interpret field measurements of ocean microstructure. In stratified channel flow, KUOM identify Ri_g as the parameter better suited for characterization of the flow. We agree. It is found that, except for a narrow region near the centreline where Ri_g is singular, the gradient Richardson number is well-behaved. Figure 20 shows the correlation coefficients associated with the momentum flux for all the simulated cases. Given the wide range of stratifications, the collapse of the different curves is good. After a relatively constant value at low values of the gradient Richardson number, the large decrease in the value of the correlation coefficient over a narrow range, $0.15 < Ri_g < 0.2$, is remarkable. This decrease in the correlation coefficient indicates a rapid change from unstratified turbulence with classical mixing characteristics to stably stratified turbulence with inhibited vertical mixing. The correlation coefficient associated with the buoyancy flux in figure 21 also shows similar features. In addition, countergradient buoyancy fluxes are present at locations with $Ri_g > 0.4$ in the strongly stratified cases, C4–C5. The vertical turbulent Froude number, Fr_w, when plotted against Ri_g in figure 16 also collapses the behaviour of the different cases. The value of Fr_w asymptotes to an $O(1)$ constant consistent with other previous observations and a scaling analysis performed for shear-driven turbulence by Sarkar (2000). Finally a closer look at figure 15 shows that two different zones can be identified, characterized by different slopes of $Ri_g(z)$,

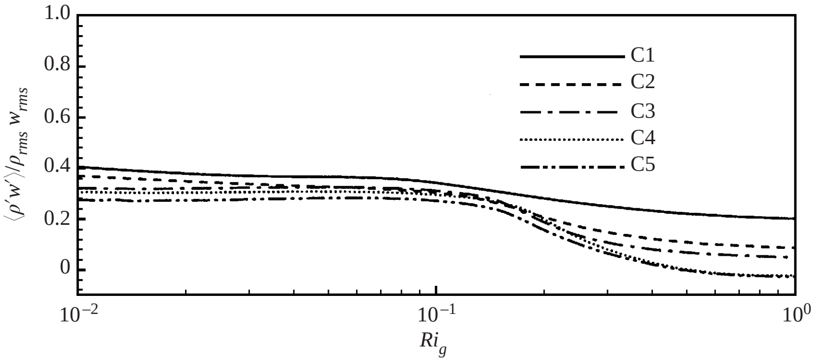

FIGURE 21. Correlation coefficient of the density flux as a function of the gradient Richardson number for several levels of stratification. Cases C1, C2, C3, C4, C5 correspond to $Ri_b = 0.032$, 0.0685, 0.112, 0.188, 0.297, respectively.

with $Ri_g \simeq 0.2$ the approximate boundary where there is a sharp change in slopes. The first zone, which corresponds to a small slope of $Ri_g(z)$, is characterized by more active turbulence and low wave activity, whereas the zone with large slope is the region where internal waves are more active and classical turbulent transport is strongly suppressed (for example look at figure 15 together with the isopycnals of figure 13). Thus, the location where the slope of $Ri_g(z)$ increases rapidly, indicates the border between the *buoyancy-dominated* central region and the *buoyancy-affected* near-wall region.

We thank Professor Linden and the late Professor Van Atta at UCSD for reading a preliminary version of the manuscript and providing helpful suggestions. The support of NSF through OCE9818912 is gratefully acknowledged. V. Armenio was also partially supported under the contract *Fluidodinamica e Analisi delle Dispersioni nella Bassissima Atmosfera del Friuli Venezia Giulia.* Computational resources at SDSC were provided through an NPACI allocation.

Appendix A. Validation of the computational model

Here, we present the results of tests performed for the validation of the computational model for both a passive scalar and stably stratified flow.

The case of a passive scalar, $Ri = 0$ in (2.2), is first investigated and results compared with data from the DNS of Kim & Moin (1989), their case II which is reported by Cabot & Moin (1993), as well as the LES results of GFMK. The LES of the passive scalar evolution is started by imposing a linear density profile on a fully developed turbulent field at $Re_\tau = 180$ and continued so that, after an initial transient, statistical convergence is achieved. Then statistics are accumulated over a non-dimensional time $u_\tau t/h \simeq 10$. A coarse grid with $48 \times 64 \times 64$ points in the streamwise, spanwise and vertical directions, respectively, as well as a grid with $64 \times 64 \times 96$ points that has improved resolution in the streamwise and vertical directions are used. The latter resolution corresponds to a ‘fine’ grid in the typical practice of LES. *A posteriori* analysis of the results shows that the Ozmidov scale $L_O = \sqrt{\epsilon/N^3}$ (with ϵ the turbulent total dissipation), which is an estimate of the smallest scale influenced by buoyancy, is generally larger than the grid spacing. Only in a very narrow region near the centreline is L_O comparable to the grid size (about

Case	Domain	Grid points	Δx^+	Δy^+	Δz^+_{min}	Δz^+_{max}
GFMK	$4\pi h \times 2\pi h \times 2h$	$64 \times 64 \times 65$	35	18	0.5	13
Current (coarse)	$4\pi h \times 4/3\pi h \times 2h$	$48 \times 64 \times 64$	47	12	1	9
Current (fine)	$4\pi h \times 4/3\pi h \times 2h$	$64 \times 64 \times 96$	35	12	1	5

TABLE 2. Summary of the computational grids used in the LES validation.

Case	Ri_τ	Re_τ	Re_b	$c_f \times 10^3$	Nu
DNS	0	180	2800	8.18	5.95
LES (GFMK)	0	180	2833	8.07	5.80
LES (coarse)	0	180	2844	8.09	6.40
LES (fine)	0	180	2822	8.14	6.30
LES (GFMK)	18	180	3084	6.81	4.0
LES (coarse)	18	180	3141	6.52	3.65
LES (fine)	18	180	3122	6.64	3.71
LES (coarse)	480	180	5133	1.22	2.39
LES (fine)	480	180	5120	1.28	2.40

TABLE 3. Summary of the final values of important bulk numbers in the simulations used for validating our LES.

0.8 the vertical grid spacing in the fine-grid case and 0.45 in the coarse-grid case). The Kolmogorov scale, η, is also small in that region, with 10η approximately the cutoff for active turbulent motion, having a value which is approximately $5L_O$. Table 2 lists the grids used in our simulations as well as the grid whose results are analysed in GMFK.

In addition to the passive scalar simulation, regridding tests using the coarse and fine grids of table 2 have been performed for $Ri_\tau = 18$ and $Ri_\tau = 480$. The coarse-grid case is initialized with a fully developed passive scalar field ($Ri_\tau = 0$) and the buoyancy term is turned on in the momentum equation. For the fine-grid case, we have interpolated the initial field from a coarse grid realization at the same Richardson number and continued the simulation until statistical steady state.

A.1. *Validation against the passive scalar case*

Velocity statistics obtained with our coarse- and fine-grid LES are compared with the DNS data of Kim & Moin (1989). Excellent agreement of the mean velocity profiles (not shown) is obtained with both grids. A more sensitive test, the resolved-scale turbulent kinetic energy K, shows that good results are obtained with both grids. Differences appear only in the buffer layer where K peaks: the coarse grid overpredicts K by 10% at $z^+ = 15$ compared to the DNS data, whereas the difference drops to 2.5% using the fine grid. Similarly to the mean velocity profile, the mean density profile also shows generally good predictions with both grids.

The final values of important overall quantities have been compared among the DNS, our LES and the LES of GFMK (table 3). For the passive scalar case, the fine-grid LES predicts a friction coefficient (c_f) that is closer to the DNS value than the LES of GFMK, whereas, for the Nusselt number the opposite is true. However the differences are small; our fine-grid Nusselt number has an over-prediction of 5.9% while GFMK underpredicts the Nusselt number by 2.5%.

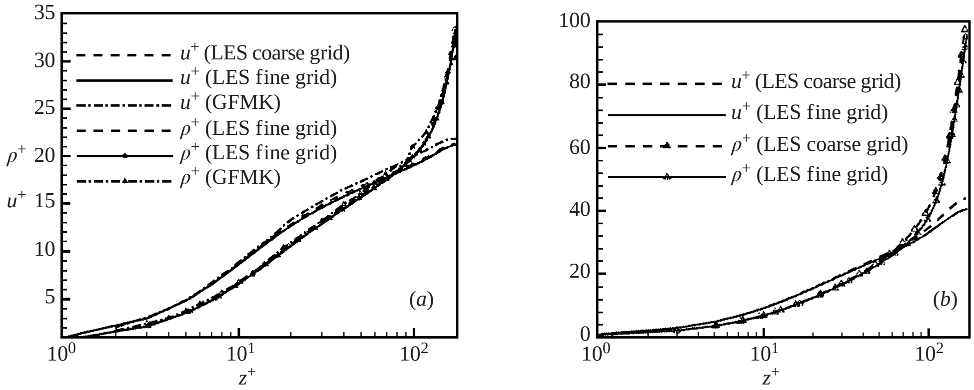

FIGURE 22. Mean velocity (curves without symbols) and mean density profiles (curves with symbols) for stratified channel flow using two grids: (*a*) $Ri_\tau = 18$ (the GFMK data are also reported); (*b*) $Ri_\tau = 480$.

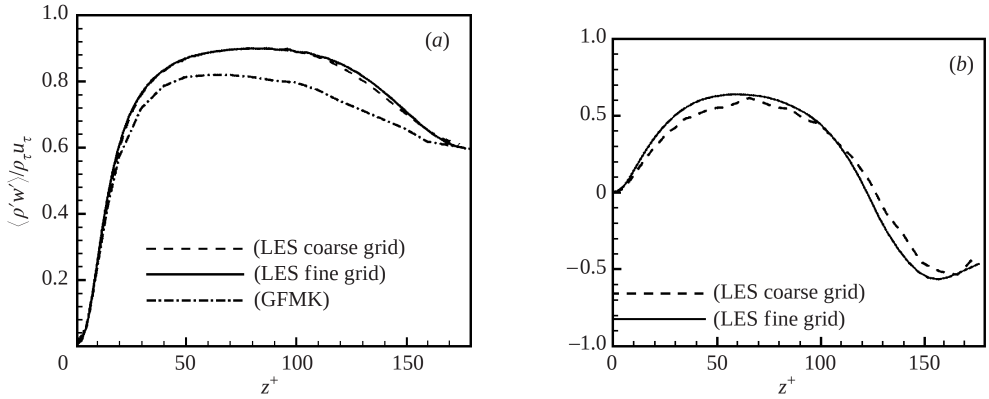

FIGURE 23. Vertical density fluxes for stratified channel flow using two grids: (*a*) $Ri_\tau = 18$ (the GFMK data are also reported); (*b*) $Ri_\tau = 480$.

A.2. *Stratified flow, regridding tests*

As mentioned previously, we have also performed regridding tests in the case of stable stratification, for $Ri_\tau = 18$ and 480. Due to the feed-back effect provided by the density field to the momentum equation, in this case the statistics of the velocity field are affected by the stratification and, therefore, it is critical to ensure that the results are not affected by the grid resolution. Figures 22 and 23 show statistics obtained with the two grids for the two levels of stratification, and the comparison with the data of GFMK obtained with their coarse grid in case C1, $Ri_\tau = 18$. This coarse grid was used by GFMK for most results pertaining to the buoyancy-affected as well as the buoyancy-dominated regime. The effect of increasing the grid resolution is small and qualitatively similar to that of the passive scalar case. In fact, the influence of the grid size on both mean velocity and mean density profiles is negligible. Our velocity and density mean profiles compare well with those of GFMK (figure 22*a*). For the turbulent kinetic energy (not shown), the results obtained with the fine grid fit those of GFMK within 6%, whereas the coarse grid predicts a peak value at $z^+ \sim 15$ larger than that of GFMK by about 13%.

Finally, the vertical density flux is quite insensitive to the grid refinements as shown

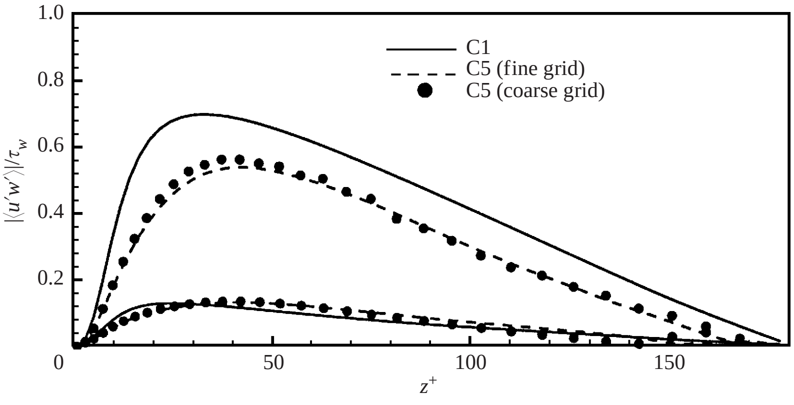

FIGURE 24. Evaluation of subgrid contribution to the Reynolds shear stress. The set of three upper curves shows the total, i.e. sum of resolved and subgrid components, while the lower curves show the subgrid components,

in figure 23 for both levels of stratification. Some differences between the present results and those of GFMK are noticeable (figure 23*a*).

Overall, although our fine and coarse grid simulations show generally small differences, the fine-grid results are systematically better, especially for the turbulent kinetic energy and wall quantities such as the skin friction and Nusselt number reported in table 3. Therefore, the fine grid is used in all the computations.

Appendix B. Performance of the subgrid model

The subgrid contributions to the momentum flux and buoyancy flux are obtained and the transport equation for K, the fluctuating kinetic energy, is examined for the weakly stratified case C1 and the strongly stratified case C5. Furthermore, an additional simulation is performed for case C5 with a different SGS model with a purely dissipative eddy viscosity.

The fluctuation of the resolved velocity is defined by $u_i'' = \bar{u}_i - \langle \bar{u}_i \rangle$. Here, $\langle . \rangle$ denotes the Reynolds average which, in channel flow, is calculated by averaging over time and the horizontal plane. The kinetic energy of the resolved scale fluctuations is denoted by $K = \langle u_i'' u_i'' \rangle$ and the resolved stress by $R_{ij} = \langle u_i'' u_j'' \rangle$.

B.1. *Subgrid contribution to the fluxes*

The upper curves in figure 24 show the total shear stress, $\langle u'w' \rangle = \langle u''w'' \rangle + \langle \tau_{13} \rangle$, while the lower curves show the subgrid stress, $\langle \tau_{13} \rangle$. Stratification does not appear to significantly affect the subgrid contribution while the total stress in case C5 is reduced with respect to case C1. Furthermore, results with the coarse grid ($48 \times 64 \times 64$) show negligible differences with the fine grid ($64 \times 64 \times 96$), as already observed by Armenio & Piomelli (2000) in neutral channel flow. The total buoyancy flux $B = \langle \rho' w' \rangle = \langle \rho'' w'' \rangle + \langle \lambda_3 \rangle$, and its subgrid component, $\langle \lambda_3 \rangle$, evaluated using the fine grid results are shown in figure 25. Countergradient (negative) flux is observed for the total buoyancy flux in the core of the channel for case C5. The subgrid buoyancy flux is non-negative because the dynamic coefficient, C_ρ, in (2.8), following standard practice, is clipped to zero whenever it becomes negative during the calculation.

The subgrid diffusivities, ν_T and k_T, are calculated using the eddy transport fluxes of momentum and buoyancy, respectively. (The scale-similarity part of the momentum

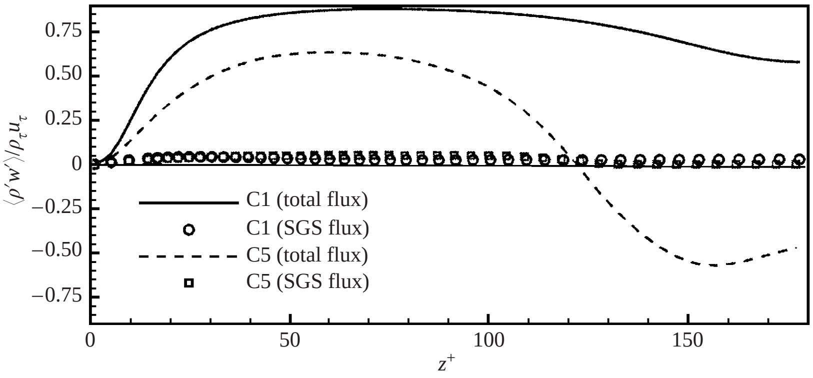

FIGURE 25. Evaluation of subgrid contribution to the buoyancy flux.

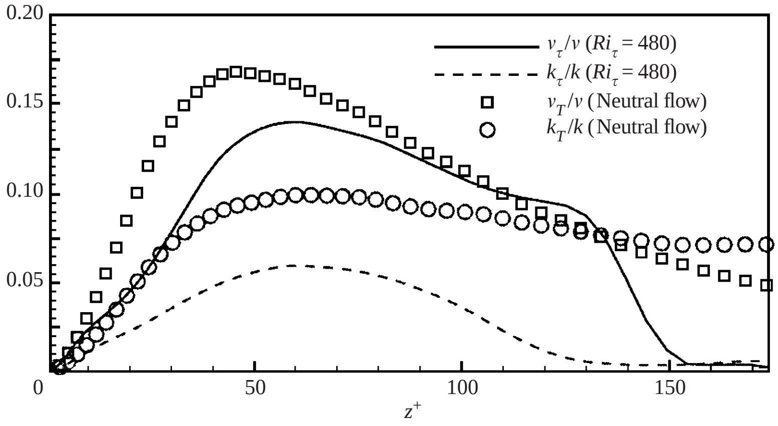

FIGURE 26. Profiles of the subgrid diffusivities of mass (k_t/k) and momentum (ν_t/ν) obtained with the mixed model: for neutral flow and for strong stratification (case C5).

flux is not used.) The vertical distributions of ν_T and k_T are reported in figure 26 both neutral flow and $Ri_\tau = 480$ (case C5). The LES cases are highly resolved in that the subgrid transport coefficients are smaller than the molecular values. As an example, for the neutral flow, the maximum value of the ratio $\nu_t/\nu \simeq 0.17$. In the case of neutral flow, the eddy diffusivities are zero at the wall and increase toward the log-zone and then slightly decrease in the core region. Such behaviour is fully consistent with that of previous LES of wall-bounded neutral flows. In the strongly stratified case, the near-wall behaviour of the eddy diffusivities is similar to that of the neutral flow, but the maximum values are reduced, in agreement with the reduced turbulent activity. In the core region, where the gradient Richardson number is large, the values of the eddy diffusivities become very small.

The subgrid Prandtl number is the ratio $Pr_{sgs} = \nu_T/k_T$ where ν_T and k_T are subgrid eddy diffusivities of momentum and buoyancy, respectively. In the neutral case, Pr_{sgs} is larger than unity in the wall region (figure 27*a*) and decreases somewhat toward the core of the channel, where turbulence is more isotropic (figure 27*b*). Such behaviour of Pr_{sgs} agrees well with previous LES of passive scalar transport, Cabot & Moin (1993) and Wang & Pletcher (1996).

In the strongly stratified case, the SGS Prandtl number behaves similarly to that of neutral flow in the near-wall region ($0 < z^+ < 30$). However, toward the centreline

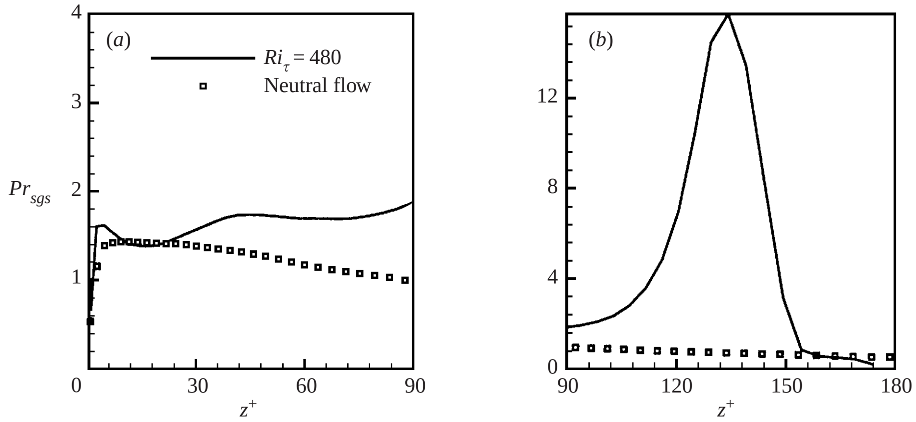

FIGURE 27. Profiles of the subgrid Prandtl number. Note that, for $z^+ > 130$, there is intermittent clipping of the dynamic constants and the subgrid diffusivities are very small, making the numerical value of their ratio, Pr_{sgs}, meaningless.

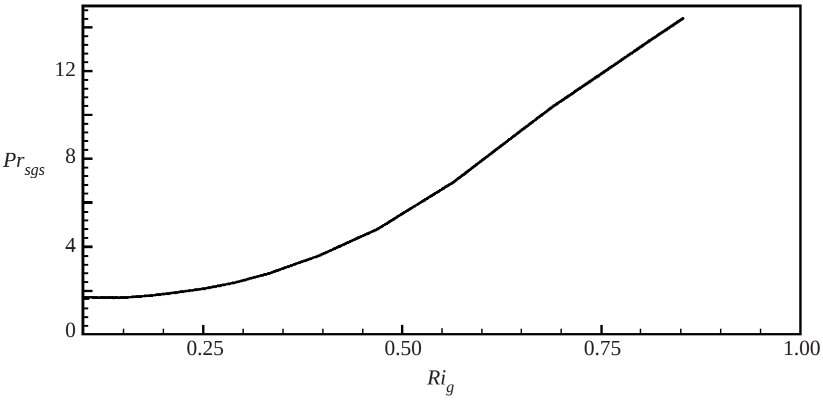

FIGURE 28. Dependence of the subgrid Prandtl number on the Richardson number, case C5 with $Ri_b = 0.297$.

($30 < z^+ < 90$), Pr_{sgs} slowly increases, and it eventually strongly increases for $100 < z^+ < 130$. Evidently, subgrid fluctuations are able to transport momentum more efficiently than buoyancy in the presence of stable stratification.

It should be noted that, near the centreline ($z^+ > 130$), the dynamic constants are intermittently clipped to zero and the correspondent eddy diffusivities are very small (see also figure 26), hence the value of Pr_{sgs}, being the ratio of two very small numbers, is not meaningful in that region.

Interestingly, Pr_{sgs} increases similarly to the gradient Richardson number (compare figure 27 with figure 15) in the strongly stratified case. Figure 28 shows Pr_{sgs} plotted as a function of Ri_g in the strongly stratified case C5. In the wall region ($z^+ < 90$) where $Ri_g < 0.2$, the SGS Prandtl number does not change significantly with increasing gradient Richardson number. In the zone $90 < z^+ < 130$, where $Ri_g > 0.2$, Pr_{sgs} rapidly increases with Ri_g. The increase is similar to that of the turbulent Prandtl number, Pr_t, in case C5, see figure 17. One difference is that, when $z^+ > 120$ and correspondingly $Ri_g > 0.48$, the total buoyancy flux becomes negative so that Pr_t cannot be defined, whereas the SGS buoyancy flux is still positive, although very small. The observed behaviour of SGS Prandtl number is consistent with the results

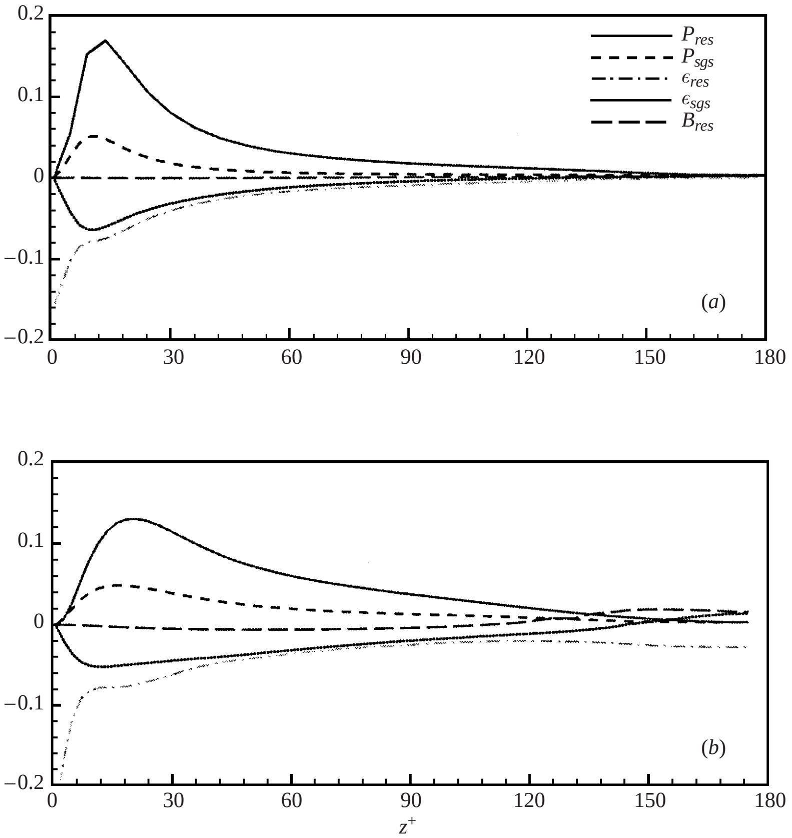

FIGURE 29. Balance of the kinetic energy showing most terms: (a) weakly stratified case, $Ri_b = 0.032$; (b) strongly stratified case, $Ri_b = 0.297$. The terms are normalized using wall-scaling, i.e. u_τ^4/ν.

shown by Schumann (1991) who propose a model which exhibits a linear increase of Pr_{sgs} with Ri_g for sufficiently large stratification. The dependence of Pr_{sgs} on stratification is not explicitly prescribed in our LES. However, it appears that the dynamic procedure automatically gives a dependence of subgrid Prandtl number on the Richardson number that is consistent with previous results.

B.2. *Budget of the resolved-scale turbulent kinetic energy*

The general transport equation for the resolved-scale turbulent kinetic energy, $K = \langle u_i'' u_i'' \rangle$, is as follows:

$$\frac{\partial K}{\partial t} + \langle \bar{u}_j \rangle \frac{\partial K}{\partial x_j} = P_{res} + P_{sgs} - \epsilon_{res} - \epsilon_{sgs} - B_{res} + \nu \nabla^2 K + \frac{\partial T_j}{\partial x_j}. \qquad \text{(B 1)}$$

Here the production has a contribution from the resolved stress, $P_{res} = -R_{ij}\langle \bar{S}_{ij} \rangle$, and from the subgrid stress, $P_{sgs} = -\langle \tau_{ij} \rangle \langle \bar{S}_{ij} \rangle$. Similarly, the dissipation rate has a viscous contribution from the resolved scales, $\epsilon_{res} = \nu \langle (\partial u_i''/\partial x_j)(\partial u_i''/\partial x_j) \rangle$, and a contribution from the SGS stress, $\epsilon_{sgs} = \langle \tau_{ij} \bar{S}_{ij} \rangle$. The resolved buoyancy flux is $B_{res} = -(g/\rho_0)\langle (\bar{\rho} - \bar{\rho}_b) w'' \rangle$. In channel flow, the terms on the left-hand side of (B 1) are zero while the terms on the right-hand side are functions of the z (or x_3)

coordinate only. The subgrid and resolved contributions to the right-hand side of (B 1) are compared and the buoyancy contribution is evaluated.

Figure 29 shows these terms for cases C1 and C5 corresponding to weak and strong stratification, respectively. In both cases, at the wall the resolved-scale dissipation ϵ_{res} is dominant while the SGS dissipation ϵ_{sgs} is zero. When $z^+ > 10$, both terms have comparable contributions to the total dissipation. The subgrid production is generally less than 30% of the resolved-scale value while the buoyancy flux, B_{res}, is very small. In the inner layer ($z^+ < 50$), stratification does not affect qualitatively turbulent production and dissipation, nevertheless it can be noticed that, as the level of stratification increases, the magnitude of these terms is noticeably reduced (i.e. the maximum resolved production is about 0.18 in C1 and it goes down to about 0.13 in C5 and similarly for the dissipation). On the other hand, the behaviour is qualitatively different in the core region, as described below. For the weakly stratified case (figure 29*a*) the profiles of the terms resemble those of a neutral flow and the buoyancy term is negligible. In the case of strongly stratified flow (figure 29*b*) the buoyancy flux is not negligible and contributes to the production of kinetic energy, consistently with the finding of the experimental investigation of KUOM. The SGS dissipation, ϵ_{sgs}, has a small positive value in the core of the flow due to the backscatter associated with the scale-similar term and acts a source of turbulent kinetic energy. However, ϵ_{sgs} is much smaller than the resolved-scale dissipation, ϵ_{res}. It should be noted that, although ϵ_{sgs} may be positive, the total dissipation $\epsilon_{sgs} + \epsilon_{res}$ remains negative (a sink for K), and monotonically decreases towards the centreline.

B.3. *Sensitivity to the subgrid model*

A main conclusion of our work is that, at the high stratification of $Ri_\tau = 480$, the flow consists of active but suppressed turbulence at the wall coexisting with a zone of internal wave activity. We emphasize that this result of a non-laminar asymptotic state is completely consistent with laboratory experiments, field measurements as well as the linear theory result that the laminar profile is unstable for this case, $Ri_\tau = 480$. Furthermore, as shown by figure 15, the region $z^+ < 90$ is subcritical with $Ri_g < 0.2$ which allows turbulence to be sustained. In spite of the supporting evidence, we have performed simulations with a different subgrid model to further strengthen our conclusion.

The scale-similar part of the SGS model allows backscatter, i.e. energy transfer from the subgrid scales to the resolved scales. In order to eliminate the possibility of turbulence being forced by subgrid scales, we performed a new simulation for case C5 ($Ri_\tau = 480$) with a purely dissipative SGS model with only dynamic eddy diffusivity models for momentum and mass, essentially switching off the scale-similar part of the original mixed model for the SGS stresses. As in the previous simulations, the eddy transport coefficients are clipped to 0 whenever they get negative. Thus, we ensure that the subgrid term is always a sink for the turbulent kinetic energy and cannot produce turbulence.

Results with the new eddy-viscosity model are close to the original results with the mixed model. In particular, the mean velocity profile (figure 30*a*) and density profile (figure 30*b*) are only slightly affected by the model and, as a consequence, profiles of the Brunt–Väisälä frequency as well as the gradient Richardson number are nearly independent of the model. The r.m.s. density fluctuations predicted with the eddy viscosity model practically coincide with those predicted with the mixed model (figure 30*c*). Both predict a small level of density fluctuations in the wall region and a high level of fluctuations in the core region. The Reynolds shear stress is nearly

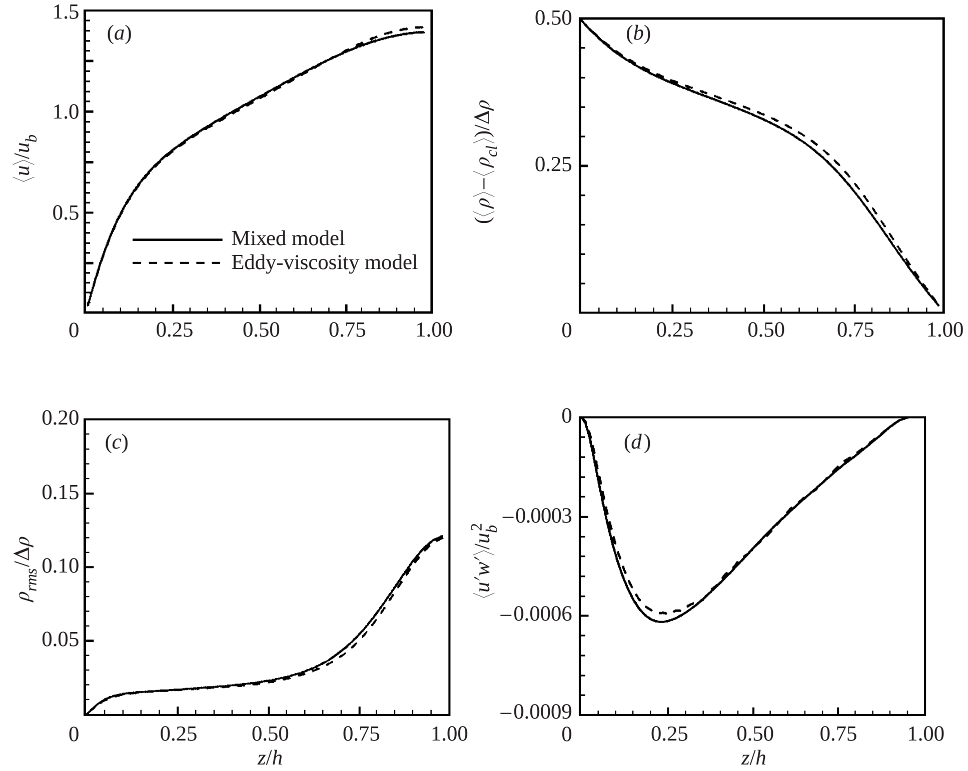

FIGURE 30. Comparison of two subgrid models in the strongly stratified case C5 with $Ri_b = 0.297$: a mixed model that allows backscatter and a purely-dissipative dynamic eddy viscosity model. (*a*) Mean velocity, (*b*) mean density, (*c*) r.m.s. density fluctuations, (*d*) Reynolds shear stress.

independent of the model (figure 30*d*) as are the normal stresses and buoyancy flux, not reported here. The visualization of the instantaneous isopycnals (not shown) at the final time of the simulation ($tu_\tau/\delta = 15.6$) clearly shows the presence of internal waves in the core of the channel just as in the previous results with the scale-similarity model. Clearly, turbulent momentum and buoyancy fluxes in the subcritical near-wall region along with internal wave activity in the core region exists at this level of stable stratification, independent of the choice of the model.

Appendix C. Influence of initialization procedure

Within the framework of an initially turbulent velocity field, we have explored a few different initialization procedures for the density field in a strongly stratified case with $Ri_\tau = 480$, $Ri_b = 0.297$. Case C5, discussed earlier in the main body of the paper, was initialized with a density field taken from the statistical steady state of case C4. The following new simulations were performed. Case C5.1 was started with a turbulent passive scalar field for the density fluctuations and the appropriate stable stratification suddenly imposed at $t = 0$ similarly to the initialization procedures for cases C1 and C2. Case C5.2 was started with zero density fluctuations and a time-dependent overall stratification that increases linearly in time from a zero value to the final value over a time period $tu_\tau/h = 20$. A time-dependent stable stratification, as in case C5.2, is probably the most relevant of these cases to geophysical flows.

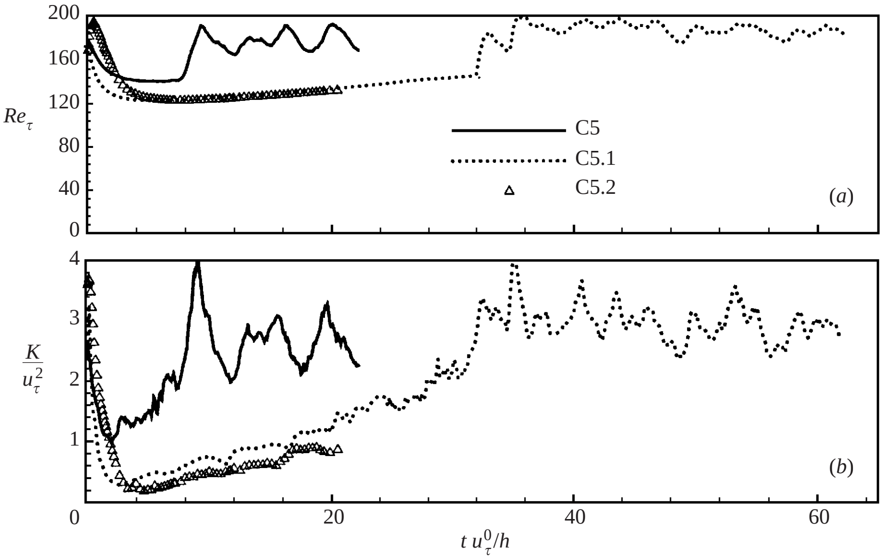

FIGURE 31. Influence of initialization procedure on the development of important bulk quantities. Note that case C5.2 was not continued to its asymptotic state.

All of these cases with initially turbulent velocity fields and final $Ri_\tau = 480$ show relaminarization during the initial transient despite the different initialization procedures for the density field. Thus, the observation of GFMK of relaminarization from turbulent initial conditions appears to be a robust feature of the initial transient although, eventually, the flow recovers to a turbulent state in the inner near-wall region due to boundary forcing.

Case C5.1 was continued for a time sufficiently long to achieve its asymptotic state. Figure 31 compares the development of two bulk quantities in cases C5 and C5.1. It is gratifying to find that the asymptotic state is approximately the same for both initialization procedures. However, the transient is significantly longer in case C5.1 that starts from a passive scalar field. In this case, the asymptotic state is obtained at $tu_\tau/h \simeq 40$ instead of the corresponding time of $tu_\tau/h \simeq 12$ for case C5. In order to avoid the computational expense of such a long transient, we initialized cases C3, C4 and C5 in the original series of simulations with a density field from cases with stable (but weaker) stratification. Turbulence statistics were also compared between the cases and differences were found to be negligible.

In order to avoid another computationally expensive simulation, case C5.2 was not continued to an asymptotic state since, after relaminarization, the evolution of bulk quantities are similar to case C5.1. Since the initialization procedures are different, the early-time transient and route to a quasi-laminar state is different. However, the development of the two cases during the recovery to turbulence is qualitatively similar.

REFERENCES

ARMENIO, V. & PIOMELLI U. 2000 A Lagrangian mixed subgrid-scale model in generalized coordinates. *Flow Turbulence Combust.* **65**, 51.

ARYA, S. P. S. 1975 Buoyancy effects in an horizontal flat-plane boundary layer. *J. Fluid Mech.* **68**, 321.

BARDINA, J., FERZIGER, J. H. & REYNOLDS W. C. 1980 Improved subgrid scale models for large eddy simulation. *AIAA Paper* 80-1357.

Britter, R. E. 1974 An experiment on turbulence in a density-stratified fluid. PhD thesis, Monash University, Australia.

Cabot, W. & Moin, P. 1993 Large eddy simulation of scalar transport with the dynamic subgrid-scale model. In *Large Eddy Simulation of Complex Engineering and Geophysical flows* (ed. B. Galperin & S. A. Orszag), p. 141. Cambridge University Press.

Caldwell, D. R. 1987 Small-scale physics of the ocean. *Rev. Geophys.* **25**, 183.

Caldwell, D. R. & Moum, J. N. 1995 Turbulence and mixing in the ocean. *Rev. Geophys.* **33**, 1385.

Caulfield, C. P. & Peltier, W. R. 2000 The anatomy of the mixing transition in homogeneous and stratified free shear layers. *J. Fluid Mech.* **413**, 1.

Crapper, P. F. & Linden, P. F. 1974 The structure of turbulent density interfaces. *J. Fluid Mech.* **65**, 45.

Diamessis, P. J. & Nomura, K. K. 2000 Interaction of vorticity, rate-of-strain, and scalar gradient in stratified homogeneous sheared turbulence. *Phys. Fluids* **12**, 1166–1188.

Gage, K. S. 1971 The effect of stable thermal stratification on the stability of viscous parallel flows. *J. Fluid Mech.* **47**, 1.

Gage, K. S. & Reid, W. H. 1968 The stability of thermally stratified plane Poiseuille flow. *J. Fluid Mech.* **33**, 21.

Garg, R. P. 1996. Physics and modeling of stratified turbulent channel flows. PhD dissertation, Stanford University.

Garg, R. P., Ferziger, J. H., Monismith S. G. & Koseff J. R. 2000 Stably stratified turbulent channel flows. I. Stratification regimes and turbulence suppression mechanism. *Phys. Fluids* **12**, 2569.

Germano, M., Piomelli, U., Moin, P. & Cabot,W. H. 1991 A dynamic subgrid-scale eddy viscosity model. *Phys. Fluids* A **3**, 1760.

Gerz, T., Schumann, U. & Elghobashi, S. E. 1989 Direct numerical simulation of stratified homogeneous turbulent shear flows. *J. Fluid Mech.* **200**, 563.

Holt, S. E., Koseff, J. R. & Ferziger, J. H. 1992 A numerical study of the evolution and structure of homogeneous stably stratified sheared turbulence. *J. Fluid Mech.* **237**, 499.

Horiuti, K. 1992 Assessment of two-equation models of turbulent passive scalar diffusion in channel flow. *J. Fluid Mech.* **238**, 405.

Ivey, G. N. & Imberger, J. 1991 On the nature of turbulence in a stratified fluid. Part 1: The energetics of mixing. *J. Phys. Oceanogr.* **21**, 650.

Jacobitz, F. G. & Sarkar, S. 1999 On the shear number effect in stratified shear flow. *Theoret. Comput. Fluid Dyn.* **13**, 171.

Jacobitz, F. G., Sarkar, S. & Van Atta, C. W. 1997 Direct numerical simulations of the turbulence evolution in a uniformly sheared and stably stratified flow. *J. Fluid Mech.* **342**, 231.

Kaltenbach, H.-J., Gerz, T. & Schumann, U. 1994 Large-eddy simulation of homogeneous turbulence and diffusion in stably stratified shear flow. *J. Fluid Mech.* **280**, 1.

Kim, J. & Moin, P. 1989 Transport of a passive scalar in a turbulent channel flow. In *Turbulent Shear Flows*, Vol. 6 (ed. J.-C. Andre *et al.*), p. 86. Springer.

Kleiser, L. & Zang, T. A. 1991 Numerical simulation of transition in wall-bounded shear flows. *Annu. Rev. Fluid Mech.* **23**, 495.

Komori, S. 1980 Turbulence structure in stratified flow. PhD Dissertation, Kyoto University.

Komori, S., Ueda, H., Ogino, F. & Mizushina, T. 1983 Turbulent structure in stably stratified open-channel flow. *J. Fluid Mech.* **130**, 13.

Koop, G. & Browand, F. K. 1979 Instability and turbulence in stratified fluids with shear. *J. Fluid Mech.* **93**, 135.

Kosovic, B. & Curry, J. A. 2000 A large eddy simulation study of a quasi-steady, stably stratified atmospheric boundary layer. *J. Atmos. Sci.* **57**, 1052.

Le Ribault, C., Sarkar, S. & Stanley, S. A. 2001 A study using large eddy simulation of the evolution of a passive scalar in a plane jet. *AIAA J.* **39**, 1509.

Lu, Y., Lueck, R. G. & Huang, D. 2000 Turbulence characteristics in a tidal channel. *J. Phys. Oceanogr.* **30**, 855.

Mason, P. J. & Derbyshire, S. H. 1990 Large eddy simulation of the stably-stratified atmospheric boundary layer. *Boundary-Layer Met.* **53**, 117.

Miles, J. W. 1961 On the stability of heterogeneous shear flows. *J. Fluid Mech.* **10**, 496.

Monin, A. S. & Obukhov, A. M. 1954 Basic laws of turbulent mixing in the ground layer of the atmosphere. *Tr. Geofiz. Inst. Akad. Nauk SSSR* **151**, 163.

Moore, M. J. & Long, R. R. 1971 An experimental investigation of turbulent stratified shearing flow. *J. Fluid Mech.* **49**, 635.

Moser, R. D., Kim, J. & Mansour, N. M. 1999 Direct numerical simulation of turbulent channel flow up to $Re_\tau = 590$. *Phys. Fluids* **11**, 943.

Panofsky, H. A. & Dutton, J. A. 1984 *Atmospheric Turbulence.* John Wiley and Sons.

Piat, J.-F. & Hopfinger, E. J. 1981 A boundary layer topped by a density interface. *J. Fluid Mech.* **113**, 411.

Piccirillo, P. S. & Van Atta, C. W. 1995 The evolution of a uniformly sheared thermally stratified turbulent flow. *J. Fluid Mech.* **334**, 61.

Rohr, J. J., Itsweire, E. C., Helland, K. N. & Van Atta, C. N. 1988 Growth and decay of turbulence in a stably stratified shear flow. *J. Fluid Mech.* **195**, 77.

Saiki, E. S., Moeng, C.-H. & Sullivan, P. P. Large-eddy simulation of the stably-stratified planetary boundary layer. *Boundary-Layer Met.* **95**, 1.

Sarkar, S. 2000 Turbulence anisotropy in stratified uniform shear flow. *Fifth Intl Symp. on Stratified Flows, Vancouver* (ed. G. A. Lawrence, R. Pieters & N. Yonemitsu), pp. 1245–1250.

Schumann, U. 1991 Subgrid length scales for large-eddy simulation of stratified turbulence. *Theoret. Comput. Fluid Dyn.* **2**, 279.

Schumann, U. & Gerz, T. 1995 Turbulent mixing in stably stratified shear flows. *J. Appl. Met.* **34**, 33.

Shih, L. H., Koseff, J. R., Ferziger, J. H. & Rehmann, C. R. 2000 Scaling and parameterization of stratified homogeneous turbulent shear flow. *J. Fluid Mech.* **412**, 1.

Smagorinsky, J. 1963 General circulation experiments with the primitive equations. I. The basic experiment. *Mon. Weath. Rev.* **91**, 99.

Smyth, W. D. & Moum, J. N. 2000 Length scales of turbulence in stably stratified mixing layers. *Phys. Fluids* **12**, 1327.

Stacey, M. T., Monismith, S. G. & Burau, J. R. 1999 Observations of turbulence in a partially stratified estuary. *J. Phys. Oceanogr.* **29**, 1950.

Staquet, C. 1995 Two-dimensional secondary instabilities in a strongly stratified shear layer. *J. Fluid Mech.* **296**, 73.

Thorpe, S. A. 1973 Experiments on instability and turbulence in a stratified shear flow. *J. Fluid Mech.* **61**, 731.

Turner, J. S. 1973 *Buoyancy Effects in Fluids.* Cambridge University Press.

Wang, W.-P. & Pletcher, R. H. 1996 On the large eddy simulation of a turbulent channel flow with significant heat transfer. *Phys. Fluids* **8**, 3354.

Wu, X. & Squires, K. D. 1997 Large eddy simulation of an equilibrium three-dimensional turbulent boundary layer. *AIAA J.* **35**, 67.

Zang, Y., Street, R. L. & Koseff, J. 1994 A non-staggered grid, fractional step method for the time-dependent incompressible Navier–Stokes equation in curvilinear coordinates. *J. Comput. Phys.* **114**, 18.